

UNIVERSITÀ DEGLI STUDI DI PAVIA
DIPARTIMENTO DI FISICA

Corso di Laurea Magistrale in Scienze Fisiche

ANALYSIS OF THE π^0 PHOTOPRODUCTION IN THE
 $\Delta(1232)$ REGION

Tesi per la Laurea Magistrale di:
GIULIA SCAFFINO

Relatore:
Dott.ssa SUSANNA COSTANZA
Correlatore:
Dott. EDOARDO MORNACCHI

Anno Accademico 2018/2019

*“The Guide is definitive.
Reality is frequently inaccurate.”*

Douglas Adams, *The Hitchhiker’s Guide to the Galaxy*

Contents

Abstract	iii
Sommario	v
1 Introduction	1
1.1 Photoexcitation and photoproduction	3
1.2 Partial wave analysis	5
1.3 Multipole expansion	7
1.4 Isospin	9
1.5 The MAID model	11
1.6 Pion photoproduction cross sections	12
2 Experimental setup	15
2.1 MAMI electron accelerator	17
2.2 Photons production	18
2.3 Glasgow Tagged Photon Spectrometer	21
2.4 Liquid hydrogen target	23
2.5 Detectors	24
2.5.1 Crystal Ball	24
2.5.2 TAPS	25
2.5.3 Particle Identification Detector	27
2.5.4 Multiwire Proportional Chambers	28
2.6 Event readout	32

3 Analysis	35
3.1 $\gamma p \rightarrow \pi^0 p$ cross section calculation	35
3.2 Software	37
3.3 Detector calibration	38
3.3.1 Tagger	38
3.3.2 Crystal Ball and TAPS	39
3.3.3 PID	41
3.4 Tagging efficiency	42
3.5 Event reconstruction	49
3.5.1 Random event subtraction	49
3.5.2 Livetime	50
3.5.3 Event selection for $\gamma p \rightarrow \pi^0 p$ reaction	50
3.6 Empty target subtraction	57
3.7 Geant4 π^0 reconstruction efficiency	57
3.8 Total inclusive cross section	59
4 Results	65
4.1 $\gamma p \rightarrow \pi^0 p$ unpolarized cross section	65
4.2 $\gamma p \rightarrow \pi^0 p$ polarized cross section	66
4.3 $p - \Delta(1232)$ transition	70
4.3.1 E2/M1 ratio	74
Conclusions	80
Acknowledgements	81
References	83

Abstract

Since many years, the internal structure of the nucleon and the excitation spectra of protons and neutrons have been the subject of intense research for many theoretical models and experiments of nuclear and particle physics.

The use of photon-induced reactions, like meson photoproduction, allow to excite the nucleon and to access many different polarisation observables which are fundamental to accurately determine the nucleon resonance properties. Furthermore, these reactions are an essential tool to extract the role of the different electromagnetic multipoles due to the presence of interference terms between different multipole amplitudes.

The A2@MAMI collaboration is carrying out a broad and systematic study on these topics, both on the proton and on the neutron. The experiments are performed at the tagged photon beam facility of the MAMI accelerator in Mainz (Germany), using unpolarized and polarized photon beams on unpolarized or longitudinally polarized proton, deuteron and ^3He targets, for energies ranging from the pion production threshold up to 1.6 GeV.

The work performed in this Master's thesis is focused on the analysis of the data collected by the A2 Collaboration at MAMI in March 2018. In the analyzed datasets, unpolarized and linearly polarized photon beams, obtained via *bremsstrahlung* on a thin amorphous and crystalline radiator respectively, were used along with an unpolarized liquid hydrogen target.

The attention has been focused on the study of the neutral pion photoproduction on the proton, in order to provide a valuable input to the study of the proton structure and its excitation spectrum.

As a first test, the total inclusive $\gamma p \rightarrow X$ cross section is studied to test the analysis accuracy and it is compared with the results of the DAPHNE collaboration, showing a good agreement.

The total and the differential $\gamma p \rightarrow \pi^0 p$ cross sections are analyzed in detail and the results are compared to the MAID2007 model predictions with a generally good agreement, both for the unpolarized and the linearly polarized photon beams.

By using the doubly-polarized pion photoproduction cross section results from the A2 collaboration, the differential cross sections for the parallel and antiparallel spin configurations have been extracted separately and compared to the MAID2007 model predictions.

Furthermore, the electric quadrupole to the magnetic dipole ratio, $R_{EM} = E2/M1$, has been calculated and determined to be $R_{EM} = - (2.5 \pm 0.28)\%$. The non-zero value of R_{EM} proves, as expected, that even though the proton is primarily photo-excited by the magnetic dipole (M1) radiation, the $p - \Delta(1232)$ transition also occurs in the presence of the electric quadrupole (E2).

Sommario

Da molti anni, la struttura interna del nucleone e, in particolare, gli spettri di eccitazione del protone e del neutrone sono stati oggetto di approfondite ricerche sia dal punto di vista teorico sia da quello sperimentale. Le reazioni nucleari indotte da foton, come la fotoproduzione di mesoni, permette di eccitare il nucleone e di accedere a diverse osservabili di polarizzazione, fondamentali al fine di determinare accuratamente le proprietà delle sue risonanze. Inoltre, grazie alla presenza di termini di interferenza tra le ampiezze dei diversi multipoli, queste reazioni costituiscono uno strumento fondamentale per comprendere il ruolo dei diversi multipoli elettromagnetici.

La collaborazione A2@MAMI sta conducendo ampi e sistematici studi su protoni e neutroni proprio in questi ambiti di ricerca. Gli esperimenti si svolgono a Mainz (Germania) presso la struttura che ospita l'acceleratore di elettroni MAMI e che è caratterizzata dalla capacità di individuare i singoli foton appartenenti ad un fascio, e quindi etichettarli. Per energie che vanno dalla soglia di produzione pionica fino a 1.6 GeV, sono disponibili fasci di foton sia polarizzati che non polarizzati e bersagli di protoni, deuterio ed ^3He polarizzati e non polarizzati.

Il lavoro svolto in questo lavoro di tesi magistrale si concentra sull'analisi dei dati raccolti dalla collaborazione A2, presso MAMI, durante il periodo di Marzo 2018. I dati analizzati provengono dall'uso di fasci di foton non polarizzati e linearmente polarizzati, ottenuti rispettivamente per *bremstrahlung* su un sottile radiatore amorfo e cristallino, e dall'utilizzo di un bersaglio di idrogeno liquido non polarizzato. L'attenzione è stata rivolta allo studio della fotoproduzione del piona neutro su protone, al fine di fornire un buon punto di partenza per lo studio della struttura del protone e del suo spettro di eccitazione.

Come prima valutazione dell'accuratezza dell'analisi, è stata studiata la sezione d'urto totale inclusiva $\gamma p \rightarrow X$ e i risultati sono stati confrontati, con un buon accordo, con quelli ottenuti in precedenza dalla collaborazione DAPHNE.

Le sezioni d'urto totale e differenziale della reazione $\gamma p \rightarrow \pi^0 p$ sono state analizzate nel dettaglio e mostrano un generale buon accordo con le previsioni del modello MAID2007,

sia per fotoni linearmente polarizzati sia per fotoni non polarizzati.

Utilizzando i risultati della sezione d’urto doppiamente polarizzata per la fotoproduzione di pioni (analisi effettuata dalla collaborazione A2), le sezioni d’urto differenziali per le configurazioni di spin parallela e antiparallela sono state separatamente estratte e confrontate con le previsioni del modello MAID2007.

In aggiunta, è stato calcolato il rapporto tra il momento di quadrupolo elettrico e il momento di dipolo magnetico, che è risultato essere pari a $R_{EM} = -(2.5 \pm 0.28)\%$. Come atteso, il valore non nullo di R_{EM} dimostra che, nonostante il protone venga principalmente eccitato da fotoni con momento di dipolo magnetico (M1), la transizione $p - \Delta(1232)$ può avvenire anche tramite l’assorbimento di fotoni con momento di quadrupolo elettrico (E2).

Chapter 1

Introduction

The Quantum Electrodynamics (QED) is a relativistic quantum field theory that describes the electromagnetic force occurring between charged particles. Along with the weak and the strong interactions, the electromagnetic interaction is a fundamental force whose carrier, also known as gauge boson, is the massless photon with spin $S = 1$. The QED describes all the interactions between point-like charged particles with an accuracy of ten parts in a billion (10^{-8}), the higher precision ever achieved for a theory. However, when non point-like particles are considered, a new theory must be introduced in order to explain their internal structure and the processes happening inside.

Here comes the Quantum Chromodynamics (QCD), a quantum field theory that describes the strong interactions occurring between quarks, point-like elementary particles that form the hadrons and the only ones carrying the colour charge (r , b and g). The strong force, for distances smaller than 0.8 fm, is mediated by eight massless gluons and its strength is independent of the colour charge. At larger scales (roughly from 1 fm to 3 fm), the strong force binds protons and neutrons together to build up nuclei via the exchange of mesons. While the high energy interactions allow a traditional perturbative expansion because of the small QCD coupling constant, at a low and intermediate energy scale the coupling constant increases and the perturbation theory does not provide any convergent solution [1].

The internal structure of nucleons, for example, has a non-perturbative nature and requires a deeper investigation. The proton and the neutron have a mass of 938.272 MeV

and 939.565 MeV respectively, but they are composed of 3 quarks each, uud for the proton and udd for the neutron, whose masses are ~ 3 MeV (up quark, u) and ~ 5 MeV (down quark, d). The quarks contribute to the nucleon mass for the 0.2% only. The non-perturbative QCD interactions are responsible for almost all the nucleon mass. Non-perturbative approaches to QCD have been developed (e.g. Chiral Perturbation Theory and quark constituent models) but the most interesting one is the lattice QCD, a gauge theory that discretizes the spacetime into a lattice of points [2, 3].

Even though a lot of efforts have been made throughout the last decades to develop valid models, some unsolved fundamental questions still exist: how many degrees-of-freedom are needed to describe the internal structure of hadrons? Moreover, how the degrees-of-freedom interact with each other? The number of nucleon resonances resulting from the models are connected to the number of degrees-of-freedom and to the quantum numbers that the models have considered. For this reason, the study of the number of excited states can disclose some important information on the number of internal degrees-of-freedom.

The number of observed resonances is much less than the theoretically predicted number, giving rise to the “missing resonances” issue. The most reliable explanation comes from the fact that the resonance overlap makes sometimes the identification really challenging. Since nucleon resonances mainly decay via the emission of mesons, their lifetime is typical of the strong interaction processes ($\tau \approx 10^{-24}$ s) and their width is of the order of 100 MeV. The gap between some resonances is of a few tens of MeV and their overlap is one of the greatest limiting factors in the resonance detection [4].

Figure 1.1 shows the total inclusive photoabsorption cross section both for the $\gamma p \rightarrow X$ and the $\gamma d \rightarrow X$ reaction, where γ is the probing photon, p is the proton, d is the deuteron and X a generic hadron. The cross sections are fitted with a smooth background and the resonances with a Breit-Wigner probability distribution, widely used in high-energy physics to describe resonances. Only the lowest excited state of the nucleon, i.e. the $P_{33}(1232)$ resonance which leads to the formation of the $\Delta(1232)$ baryon with a mass equal to 1232 MeV, presents an isolated peak in the spectrum; for energies near 1500 MeV, the $P_{11}(1440)$, $D_{13}(1520)$, and $S_{11}(1535)$ resonances, whose masses are 1440 MeV, 1520 MeV and 1535 MeV respectively, take part to the second resonance region and a

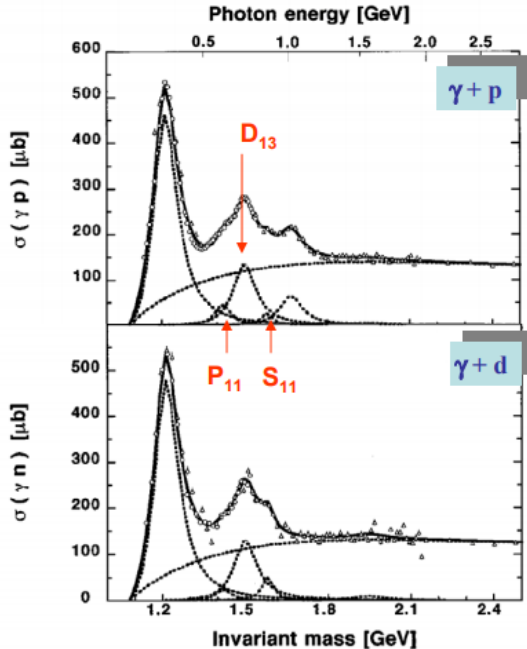


Figure 1.1: The total inclusive photoabsorption cross section both for the $\gamma p \rightarrow X$ and the $\gamma d \rightarrow X$ reaction. The cross sections are fitted with a smooth background and the resonances with a Breit-Wigner distributions [4].

detailed study of all those closely spaced resonances is prohibitive. A third resonance region is also evident.

1.1 Photoexcitation and photoproduction

The dataset of physical observables describing the nucleon properties comes from a wide variety of different scattering experiments, performed by using both hadronic and electromagnetic probes. Concerning the hadronic probes, especially protons and pions, the cross sections are much higher than in the electromagnetic case. Nevertheless, the reactions exhibit a greater complexity because of the strong interactions occurring within the initial state.

It is usually more convenient to deal with electrons or photons instead of hadrons because of the complete knowledge of the whole reaction (the electromagnetic vertex is completely understood), despite of the lower cross sections and of the large non-resonant background contribution.

The photoproduction processes are of especial interest for this work: they consist of meson production induced by the interaction between high-energy photons and hadrons,

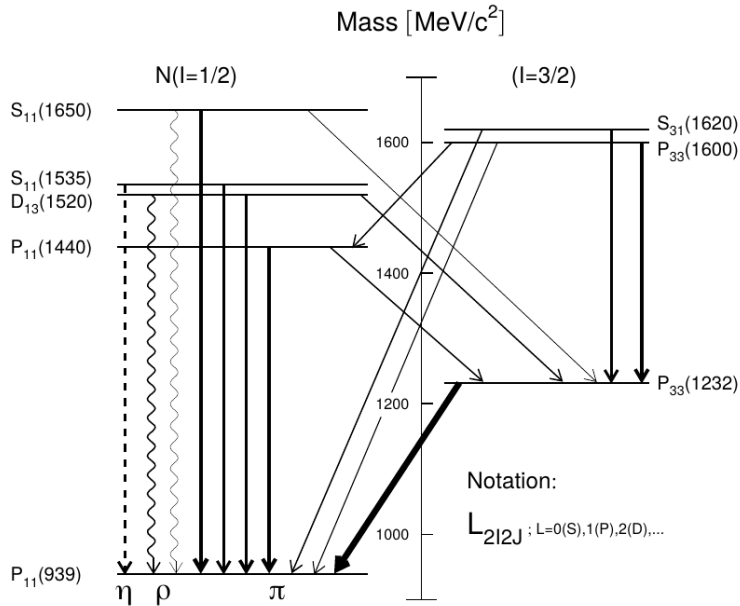


Figure 1.2: The low energy excited states of the nucleon and the main transitions via meson emissions. On the left hand side: N^* excited states with isospin $I = \frac{1}{2}$. On the right hand side: Δ excited states with isospin $I = \frac{3}{2}$. The solid, dashed and curled arrows represents the decay via pion meson emission, η meson emission and ρ meson emission, respectively [4].

in our case protons. Electromagnetic probes allow for the investigation of form factors, polarizabilities and helicity amplitudes, which are otherwise impossible to measure.

Figure 1.2 summarizes the low energy excited states of the nucleon and the main transitions via meson emission. On the left hand side, there are the N^* excited states with isospin $I = \frac{1}{2}$ and, on the right hand side, the Δ excited states with isospin $I = \frac{3}{2}$. The solid, dashed and curled arrows represents the decay via pion meson emission, η meson emission and ρ meson emission respectively. The more the lines are thick, the higher the branching ratios are. The excited states are labeled with the standard notation $L_{2I2J}(W)$ where W is the mass, $L = 1, 2, 3 = S, P, D$ is the angular momentum of the final meson-nucleon pair. I and J are the spin and isospin respectively. Photoproduction of pions is the most examined channel so far and it can occur via the excitation of both N^* and Δ resonance states.

In the following sections, the partial wave analysis method will be discussed because of its relevance for isolating contributions from different resonances.

1.2 Partial wave analysis

The scattering problems are usually solved by using the partial wave analysis (PWA) method, which consists of decomposing the wave function into different angular momentum contributions, namely partial waves or multipoles, and then analyse their amplitudes. Each partial wave has its own scattering amplitude that can be independently analyzed.

The pion photoproduction on a proton can be written as:

$$\gamma(\mathbf{k}, \lambda_\gamma) + N(\mathbf{p}, \lambda) \rightarrow \pi(\mathbf{q}) + N'(\mathbf{p}', \lambda), \quad (1.1)$$

where λ is referred to helicities, \mathbf{k} and \mathbf{q} stand for the photon and pion momentum, respectively, and \mathbf{p} and \mathbf{p}' are the proton momenta before and after the interaction. The pion has spin zero.

For a given reaction, the information on the amplitude value lies within the T-matrix that is the transition matrix that connects initial and final states. The amplitude for the photoproduction of a pseudoscalar meson (in this case a pion) is described by the following matrix element:

$$T_{fi} = \langle \mathbf{q}, \nu_f | T | \mathbf{k}, \lambda_\gamma, \nu_i \rangle \equiv \langle f | \mathcal{F} | i \rangle = \langle f | J_\mu \epsilon_\lambda^\mu | i \rangle, \quad (1.2)$$

where $|i\rangle$ and $|f\rangle$ are the initial and final states, ν_i and ν_f are the initial and final spinors of the nucleon that contains the spin information, \mathcal{F} is the transition amplitude matrix, J_μ represents the current density in standard QED and ϵ_λ^μ is the photon polarization vector. The four-vector J_μ combines the charge density and the spatial current density [5]:

$$J^\mu = (J^0, \mathbf{J}) = (c\rho, \mathbf{J}). \quad (1.3)$$

It is possible to describe J_μ in a Lorentz invariant and gauge invariant parametric form [6]:

$$J_\mu = i\mathcal{F}_1 \sigma_\mu + \mathcal{F}_2 \frac{\epsilon_{\mu ij} \sigma_i k_j}{|\mathbf{k}| |\mathbf{q}|} + i\mathcal{F}_3 \frac{\sigma \mathbf{k}}{|\mathbf{k}| |\mathbf{q}|} q_\mu + i\mathcal{F}_4 \frac{\sigma \mathbf{q}}{\mathbf{q}^2} q_\mu, \quad (1.4)$$

and, in particular, the spatial component can be written in the following way:

$$\mathbf{J} = i\mathcal{F}_1 \boldsymbol{\sigma} + \mathcal{F}_2 (\boldsymbol{\sigma} \cdot \hat{\mathbf{q}})(\boldsymbol{\sigma} \times \hat{\mathbf{k}}) + i\mathcal{F}_3 (\boldsymbol{\sigma} \cdot \hat{\mathbf{k}}) \hat{\mathbf{q}} + i\mathcal{F}_4 (\boldsymbol{\sigma} \cdot \hat{\mathbf{q}}) \hat{\mathbf{q}}. \quad (1.5)$$

The \mathcal{F}_i are the commonly named Chew-Goldberger-Low-Nambu (CGLN) amplitudes and they can be expressed as a function of the scattering angle [7, 8]:

$$\mathcal{F}_1(z) = \sum_{L=0}^{\infty} [LM_L^+ + E_L^+] P'_{L+1}(z) + [(L+1)M_L^- + E_L^-] P'_{L-1}(z) \quad (1.6)$$

$$\mathcal{F}_2(z) = \sum_{L=1}^{\infty} [(L+1)M_L^+ + LM_L^-] P'_L(z) \quad (1.7)$$

$$\mathcal{F}_3(z) = \sum_{L=1}^{\infty} [E_L^+ - M_L^+] P''_{L+1}(z) + [E_L^- + M_L^-] P''_{L-1}(z) \quad (1.8)$$

$$\mathcal{F}_4(z) = \sum_{L=2}^{\infty} [M_L^+ - E_L^+ - M_L^- - E_L^-] P''_L(z). \quad (1.9)$$

L represents the orbital angular momentum in the πp system, $P_L(z)$ are the Legendre polynomials with $z = \mathbf{k}\mathbf{q}/(|\mathbf{k}||\mathbf{q}|)$ and E_L^\pm and M_L^\pm are the electric and magnetic multipole describing the transitions to states with $J = L \pm \frac{1}{2}$. These amplitudes can be further expanded in electric and magnetic multipoles.

The transition amplitude \mathcal{F} can be finally defined as:

$$\mathcal{F} = i\mathcal{F}_1(\boldsymbol{\sigma} \cdot \boldsymbol{\epsilon}) + \mathcal{F}_2(\boldsymbol{\sigma} \cdot \hat{\mathbf{q}})(\boldsymbol{\sigma} \cdot (\hat{\mathbf{k}} \times \boldsymbol{\epsilon})) + i\mathcal{F}_3(\boldsymbol{\sigma} \cdot \hat{\mathbf{k}})(\hat{\mathbf{q}} \cdot \boldsymbol{\epsilon}) + i\mathcal{F}_4(\boldsymbol{\sigma} \cdot \hat{\mathbf{q}})(\hat{\mathbf{q}} \cdot \boldsymbol{\epsilon}). \quad (1.10)$$

By using an unpolarized target and an unpolarized photon beam, it is possible to measure the unpolarized differential cross section. In the center of mass frame, the unpolarized differential cross section can be described as a function of the CGLN amplitudes [4]¹:

$$\begin{aligned} \frac{\mathbf{k}^*}{\mathbf{q}^*} \frac{d\sigma}{d\Omega} = & \left[|\mathcal{F}_1|^2 + |\mathcal{F}_2|^2 + \frac{1}{2}|\mathcal{F}_3|^2 + \frac{1}{2}|\mathcal{F}_4|^2 + \text{Re}(\mathcal{F}_1\mathcal{F}_3^*) \right] \\ & + [\text{Re}(\mathcal{F}_3\mathcal{F}_4^*) - 2\text{Re}(\mathcal{F}_1\mathcal{F}_2^*)] \cos \Theta^* \\ & - \left[\frac{1}{2}|\mathcal{F}_3|^2 + \frac{1}{2}|\mathcal{F}_4|^2 + \text{Re}(\mathcal{F}_1\mathcal{F}_4^*) + \text{Re}(\mathcal{F}_2\mathcal{F}_3^*) \right] \cos^2 \Theta^* \\ & - [\text{Re}(\mathcal{F}_2\mathcal{F}_4^*)] \cos^3 \Theta^* \end{aligned}$$

with Θ^* representing the polar angle of the outgoing meson in the center of momentum frame. From the four \mathcal{F}_i complex amplitudes, it is possible to construct 16 bilinear products, i.e. 16 polarization observables for every fixed value of energy and angle (E, Θ). Together with the unpolarized cross section, there are 3 single polarization

¹The starred variables are evaluated in the center of mass frame.

Photon polarization		Target polarization	Recoil nucleon polarization	Target and recoil polarization
		X Y Z _(beam)	X' Y' Z'	X' X' Z' Z' X Z X Z
unpolarized linear circular	σ $-\Sigma$ -	- T - H (-P) -G F - -E	- P - O _{X'} (-T) O _{Z'} C _{X'} - C _{Z'}	T _{X'} L _{X'} T _{Z'} L _{Z'} (-L _{Z'}) (T _{Z'}) (L _{X'}) (-T _{X'}) - - - - -

Table 1.1: Polarization observables [9]. In red the double polarization observables, in blue the single polarization observables and in green the unpolarized one.

observables and 12 double polarization observables, which are classified depending on the beam, target or recoil nucleon polarization [9]. All the polarization observables are summarized in Table 1.1. In red are shown the double polarization observables, in blue the single polarization observables and in green the unpolarized one.

Therefore, in order to carry out a “complete experiment” and yield a model-independent analysis, the measurement of 8 properly chosen observables is necessary [10, 11].

1.3 Multipole expansion

Since the aim of this project consists of an experimental analysis of the pion photoproduction, it is worthwhile to remember the multipole expansion and some rising selection rules. The meson photoproduction resulting from the excitation of an intermediate state (a resonance) will be discussed in the following because of its key role in the investigation of the excited state properties.

As Figure 1.3 shows, an initial state composed of a photon and a nucleon is considered. The photon has a total angular momentum $\vec{L}_\gamma = \vec{l}_\gamma + \vec{s}_\gamma$, with \vec{l}_γ being its orbital angular momentum respect to the target nucleon and $\vec{s}_\gamma = 1$ its intrinsic spin, and a defined parity P_γ . The nucleon has spin $\vec{J}_N = \frac{1}{2}$ and even parity $P_N = +1$. When they are close enough to interact with each other, a resonance state with spin \vec{J}_{N^*} and parity P_{N^*} comes up and then it decays into a pion and the spectator nucleon. The pion has a orbital momentum \vec{L}_π respect to the nucleon and a parity P_π . In the multipole expansion

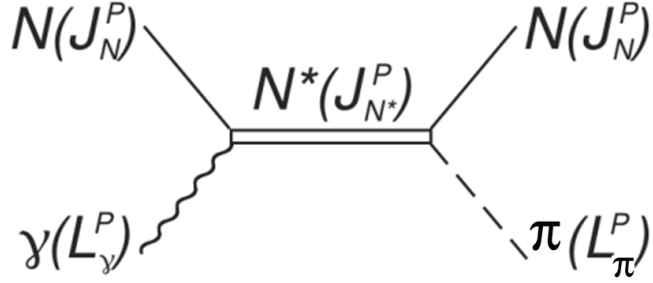


Figure 1.3: Sketch of a meson photoproduction (γp) process with the formation of an intermediate resonant state [4].

of the gamma radiation, the electric (E) and magnetic (M) multipoles are usually defined by the angular momentum L and are therefore labeled as EL and ML . Electric and magnetic multipoles have different selection rules as concern parity and it follows that, once the initial and final states are selected, both an electric and a magnetic transitions having the same multipolarity can not occur:

$$EL : \quad P_\gamma = (-1)^L \quad (1.11)$$

$$ML : \quad P_\gamma = (-1)^{L+1}. \quad (1.12)$$

The reaction is fixed by the following selection rules [4]:

$$|L_\gamma - J_N| = |L_\gamma - \frac{1}{2}| \leq J_{N*} \leq |L_\gamma + \frac{1}{2}| = |L_\gamma + J_N| \quad (1.13)$$

$$P_\gamma \cdot P_N = P_\gamma = P_{N*}. \quad (1.14)$$

The resonant state is unstable and, through the emission of a pion (spin $\vec{s}_\pi = 0$, parity $P_\pi = -1$ and relative orbital angular momentum L_π), it decays into its ground state with a lifetime typical of the strong interaction ($\tau \approx 10^{-24}$ s). The selection rules for the decay process are:

$$|L_\pi - J_N| = |L_\pi - \frac{1}{2}| \leq J_{N*} \leq |L_\pi + \frac{1}{2}| = |L_\pi + J_N| \quad (1.15)$$

$$P_{N*} = P_N \cdot P_\pi \cdot (-1)^{L_\pi} = (-1)^{L_\pi+1}. \quad (1.16)$$

By combining Equation (1.13) with (1.15) and Equation (1.14) with (1.16), the following properties of the intermediate state appear:

$$P_{N^*} = P_\gamma = (-1)^{L_\pi+1} \quad (1.17)$$

$$J_{N^*} = L_\pi \pm \frac{1}{2} = L_\gamma \pm \frac{1}{2}, \quad (1.18)$$

where the two solutions denoted by the \pm symbols are independent. The parity and the total momentum conservation laws establish for the initial photon two different selection rules [4]:

$$EL : \quad L = L_\pi \pm 1 \quad (1.19)$$

$$ML : \quad L = L_\pi. \quad (1.20)$$

The photoproduction multipoles for pseudo-scalar mesons are designated as $E_{l\pm}$ and $M_{l\pm}$, where E and M are referred to the electric and magnetic photon multipoles, $l = L_\pi$ is the relative angular momentum of the final πN system and the signs '+' or '-' specify if the nucleon spin must be subtracted or added to l in order to give the correct total angular momentum J_{N^*} of the resonant state.

For example, in the interest of this work, one considers the absorption of the E_{1+} transition multipole (connected to the P wave, $L = 1$) that excites the $\Delta(1232)$ intermediate state with $I = \frac{3}{2}$, whose dominant decay channel is the P-wave pion emission. From Equation (1.20), it follows that the absorbed initial photon must have an angular momentum of $L = 2$ and it is therefore a $E2$ photon multipole (electric quadrupole). Even the M_{1+} transition moment can excite the $J^P = \frac{3}{2}^+$ resonance but, in this case, the initial photon must have $L = 1$ and it is a $M1$ photon multipole (magnetic dipole). Table 1.2 summarizes some multipole amplitudes for the meson photoproduction reactions.

1.4 Isospin

The isospin I or, more precisely, the isobaric spin, is a dimensionless quantum number associated with the strong nuclear force and conserved in strong interaction decays. The charge independence of the strong force results from the invariance under unitary transformations in the isospin space. Such a transformation coincides with replacing

L_γ	γ multipole	J	P	Transition multipole	Resonance
1	E1	1/2	-	E ₀₊	S ₁₁
1	E1	3/2	-	E ₂₋	D ₁₃
1	M1	1/2	+	M ₁₋	P ₁₁
1	M1	3/2	+	M ₁₊	P ₃₃
2	E2	3/2	+	E ₁₊	P ₃₃
2	E2	5/2	+	E ₃₋	F ₁₅
2	M2	3/2	-	M ₂₋	D ₁₃
2	M2	5/2	-	M ₂₊	D ₁₅

Table 1.2: Multipole amplitudes for some meson photoproduction reactions [4].

protons with neutrons and vice versa [1].

As already pointed out in Section 1.1, the pion photoproduction may arise from both the N* and the Δ intermediate states. Since the electromagnetic interaction does not respect the isospin conservation, the Hamiltonian describing the photoproduction process presents both isoscalar ($\Delta I = 0$) and isovector ($\Delta I = 0, \pm 1$) components. The pion photoproduction on a nucleon must be therefore described by considering all the four different $|I, I_3\rangle$ states of isospin (I_3 is the third component of the isospin):

$$|p\rangle = \left| \frac{1}{2}, +\frac{1}{2} \right\rangle, \quad |n\rangle = \left| \frac{1}{2}, -\frac{1}{2} \right\rangle, \quad |\pi^-\rangle = |1, -1\rangle, \quad |\pi^0\rangle = |1, 0\rangle, \quad |\pi^+\rangle = |1, +1\rangle.$$

The final πN states are defined by using the Clebch-Gordan coefficients [12]:

$$|\pi^- p\rangle = \sqrt{\frac{1}{3}} \left| \frac{3}{2}, -\frac{1}{2} \right\rangle - \sqrt{\frac{2}{3}} \left| \frac{1}{2}, -\frac{1}{2} \right\rangle \quad (1.21)$$

$$|\pi^0 p\rangle = \sqrt{\frac{2}{3}} \left| \frac{3}{2}, +\frac{1}{2} \right\rangle - \sqrt{\frac{1}{3}} \left| \frac{1}{2}, +\frac{1}{2} \right\rangle \quad (1.22)$$

$$|\pi^+ p\rangle = - \left| \frac{3}{2}, +\frac{3}{2} \right\rangle \quad (1.23)$$

$$|\pi^- n\rangle = + \left| \frac{3}{2}, +\frac{3}{2} \right\rangle \quad (1.24)$$

$$|\pi^0 n\rangle = \sqrt{\frac{2}{3}} \left| \frac{3}{2}, -\frac{1}{2} \right\rangle + \sqrt{\frac{1}{3}} \left| \frac{1}{2}, -\frac{1}{2} \right\rangle \quad (1.25)$$

$$|\pi^+ n\rangle = - \sqrt{\frac{1}{3}} \left| \frac{3}{2}, +\frac{1}{2} \right\rangle - \sqrt{\frac{2}{3}} \left| \frac{1}{2}, -\frac{1}{2} \right\rangle. \quad (1.26)$$

The 1.23 and 1.24 states cannot be the result of a photoproduction process because of the $I_3 = \frac{3}{2}$ third component.

1.5 The MAID model

Some theoretical models are based on partial wave analysis. One of them is the MAID Unitary Isobar Model, which dates back to the 1998, when it was composed of a small set of nucleon resonances described with Breit-Wigner distributions and a non-resonant background [13].

In this work, the analysis results will be compared to the predictions of the MAID2007 updated version. It collects a big dataset of the pion photoproduction and pion electroproduction on nucleons, providing predictions on a wide range of observables and including information on proton and neutron resonances up to 2.00 GeV. MAID2007, in particular, contains multipoles up to $L \leq 5$, where L is the angular momentum between the pion and the nucleon. The MAID2007 model is accessible online [14].

The MAID2007 model considers the transition matrix T in the form [13]:

$$T_{\gamma\pi}(M_r) = V_{\gamma\pi}(M_r) + V_{\gamma\pi}(M_r) g_0(M_r) T_{\pi N}(M_r), \quad (1.27)$$

where $V_{\gamma\pi}$ is the $\gamma N \rightarrow \pi N$ transition potential, $T_{\pi N}$ is the πN scattering matrix, g_0 stands for the free πN propagator and M_r for the resonance mass. In a resonant region,

the transition potential $V_{\gamma\pi}$ comprehends the non-resonant background term $V_{\gamma\pi}^B$ and the isolated contribution of the resonance $V_{\gamma\pi}^R$:

$$V_{\gamma\pi}(M_r) = V_{\gamma\pi}^B(M_r) + V_{\gamma\pi}^R(M_r). \quad (1.28)$$

It follows that the T matrix can be also decomposed in two different contributions:

$$T_{\gamma\pi}^B(M_r) = V_{\gamma\pi}^B(M_r) + V_{\gamma\pi}^B(M_r) g_0(M_r) T_{\pi N}(M_r), \quad (1.29)$$

$$T_{\gamma\pi}^R(M_r) = V_{\gamma\pi}^R(M_r) + V_{\gamma\pi}^R(M_r) g_0(M_r) T_{\pi N}(M_r). \quad (1.30)$$

$$(1.31)$$

The multipoles can be therefore described as:

$$E_{l\pm} = E_{l\pm}^B + E_{l\pm}^R, \quad (1.32)$$

$$M_{l\pm} = M_{l\pm}^B + M_{l\pm}^R. \quad (1.33)$$

Both the non-resonant and the resonant terms have some free parameters that can be inferred by the data distribution.

1.6 Pion photoproduction cross sections

The work presented in the following chapters analyses the data collected by the A2 collaboration of Mainz during the data-taking period of March 2018. It is focused on the calculation of the total and differential cross section of the $\gamma p \rightarrow \Delta(1232) \rightarrow \pi^0 p$ reaction. In addition, the E_{1+} multipole contribution to the P_{33} resonance (that lead to the formation of the $\Delta(1232)$ baryon) will be estimated by using also the cross section results of the polarized $\vec{\gamma}p \rightarrow \Delta(1232) \rightarrow \pi^0 p$ reaction, analyzed within the A2 collaboration (Prof. P. Pedroni) and not published yet.

Figure 1.4 exhibits the MAID predictions for the unpolarized total cross section (on the left hand side) and the polarized total cross section $\Delta\sigma = \sigma_{3/2} - \sigma_{1/2}$ (on the right hand side), where $\sigma_{3/2}$ and $\sigma_{1/2}$ represent the parallel and antiparallel spin configuration of the photon and the proton. The contribution of different multipoles is also outlined.

It is clear that the study of the different multipole contributions is quite prohibitive in the unpolarized reaction because the transition is almost completely given by the M_{1+}

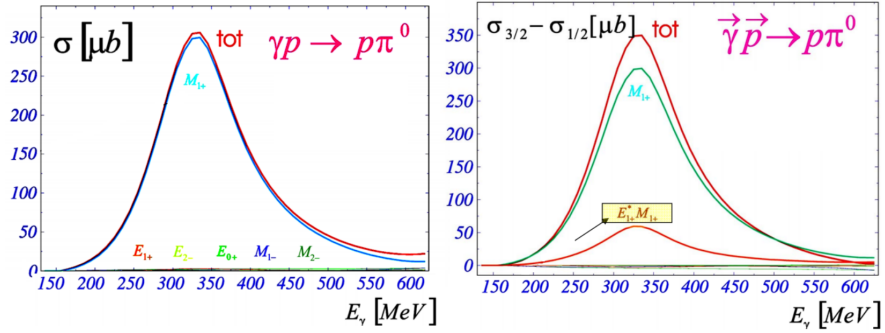


Figure 1.4: MAID predictions of the unpolarized total cross section (left) and the polarized total cross section $\Delta\sigma = \sigma_{3/2} - \sigma_{1/2}$ (right), where $\sigma_{3/2}$ and $\sigma_{1/2}$ represent the parallel and antiparallel spin configuration of the photon and the proton. The contributions of different multipoles is also outlined. [15].

multipole and no other contribution is large enough to allow an experimental evaluation. The polarized cross section, instead, along with the dominant M_{1+} multipole contribution, manifests a non-negligible term resulting from the interference of the M_{1+} and E_{1+} multipoles. This interference term will be of decisive importance in the evaluation of the E_{1+} involvement in the nuclear reaction.

Chapter 2

Experimental setup

The data analyzed in my thesis were collected at the MAMI-A2 tagged photon facility in Mainz (Germany) during a three weeks run period in March 2018 and the following chapter outlines the experimental setup.

To study the π^0 photoproduction, a photon beam and a proton target are required. The photon beam is produced via *bremssstrahlung* on a thin radiator, starting from the electron beam of the Mainz Microtron (MAMI), with an energy of 883 MeV. Outgoing electrons were bent by a magnetic dipole and detected using the Tagged Photon Spectrometer (Tagger). The Tagger plays an important role both for the calculation of the energy of the photons and for the timing coincidence between Tagger and trigger. In fact, the energy of photons was inferred by a momentum analysis of the *bremssstrahlung* electrons based on which is the Tagger channel that fires. The photon beam was then collimated and headed towards an unpolarized 10 cm liquid hydrogen (LH_2) target located in the centre of the detection system. Detection of final state particles was carried out using a Particle Identification Detector (PID) to provide particle identification, two Multiwire Proportional Chambers (MWPCs) to provide accurate position information for charged particles, Crystal Ball (CB) calorimeter with a roughly 4π angular coverage and TAPS to give calorimetry, tracking and identification in the forward region.

The arrangement of these detectors can be seen in Figure 2.1.

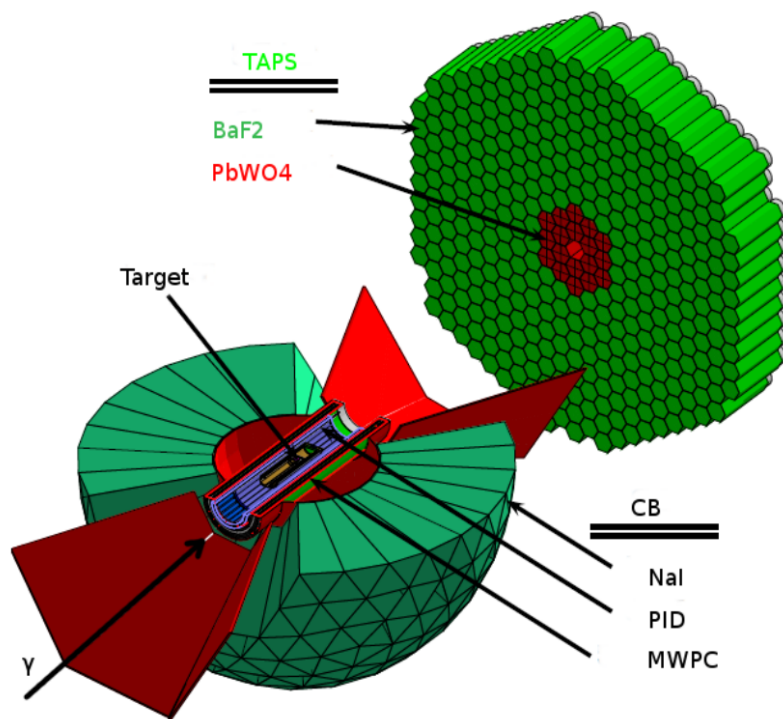


Figure 2.1: The detectors setup in the A2 hall, showing the MWPCs and PID inside the Crystal Ball, and TAPS covering the downstream region [16].

2.1 MAMI electron accelerator

MAMI, the MAinzer MIcrotron, is a three-stage racetrack microtron (RTM) with 100% duty factor, capable of providing continuous wave electron beams (polarized or unpolarized) with energies up to 1.5 GeV.

Electrons are obtained by thermoionic emission and are accelerated up to 4.1 MeV via a LINAC injector. After this stage, electrons enter a cascade of 3 racetrack microtrons. As shown in Figure 2.2, a microtron is an accelerator in which the electron beam is re-circulated many times through both a single LINAC and focusing devices, using two constant-field dipole magnets that bend electrons by 180°. As the electron energy increases, the radius of curvature of the path through the bending magnets increases. Thus, each successive recirculation loop becomes larger, with the common point of contact being the path through the accelerating section of the microtron. When the beam has been accelerated to the desired energy, a small “kicker” magnet ejects it out of the recirculation pathway into the beam handling system. The difference in time between each successive recirculation loop has to be an exact integer multiple of the RF period so that the particle bunches always see the same phase of the alternating voltage in the accelerating section.

The three racetrack microtrons of MAMI have final ejection energies of 15.3 MeV, 185.9 MeV and 883 MeV, respectively. The microtron provides exceptional phase stability and small energy spread of the final beam due to its inherent phase correction. Particles travelling in the bunch that have more than the designed energy will have a longer path through the bending magnets and will arrive at the accelerating section later than the rest of the bunch; hence, they will be under-accelerated in the next re-circulation. Particles with less than the designed energy will follow a shorter orbit: they will arrive earlier and they will be over-accelerated. The continual under/over acceleration of particles, coupled with continual energy loss due to synchrotron radiation, keeps the energy spread to the minimum.

For energies higher than 883 MeV, the use of a microtron becomes prohibitive because of the increased size of the dipole magnets required to bend charged particles. Energies up to 1.5 GeV are provided by the Harmonic Double Sided Microtron (HDSM) via four

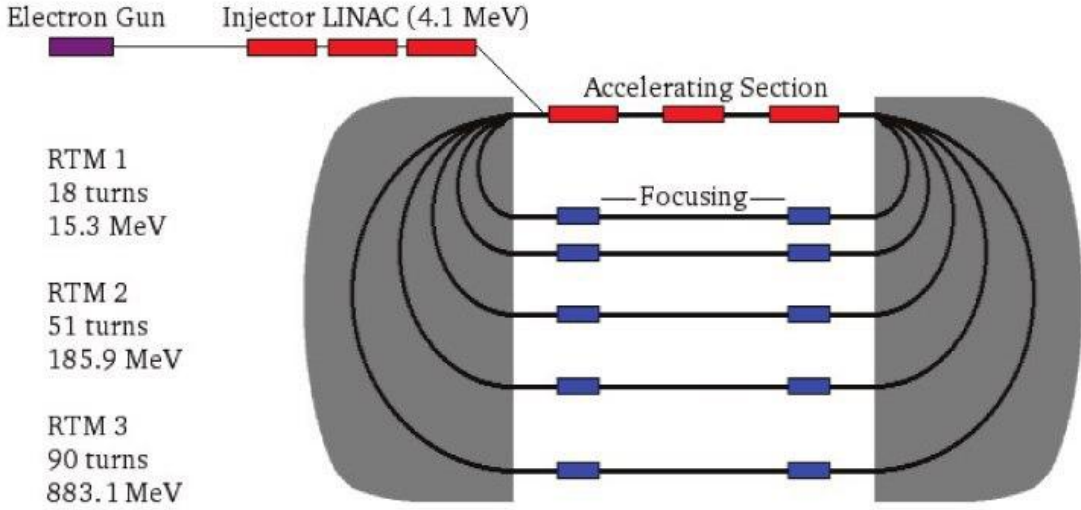


Figure 2.2: A microtron accelerates electrons by re-circulating them many times through both a single LINAC and focusing devices. It uses two constant-field dipole magnets that bend electrons by 180°. The three racetrack microtrons of MAMI have final ejection energies of 15.3 MeV, 185.9 MeV and 883 MeV respectively [17].

dipole magnets, as shown in Figure 2.3. Each magnet has to bend electrons by 90° only and the size of individual magnets is thereby reduced; moreover, the HDSM includes two LINAC accelerating sectors rather than a single one. When the electron beam achieves the desired energy value, particles are extracted and are sent to one of the experimental halls of the facility, as shown in Figure 2.4.

2.2 Photons production

Bremsstrahlung occurs when an electron interacts with the Coulombian field of a radiator's nucleus and a photon is thus emitted giving momentum to the whole atom:

$$e^- N \longrightarrow e^-' N' \gamma.$$

Since the *bremsstrahlung* cross section depends on the atomic number Z as Z^2 , when the MAMI electron beam enters the A2 hall, it impinges upon a thin radiator of high- Z material in order to achieve high photon fluxes. Three different radiators were used during the runs analyzed in this thesis:

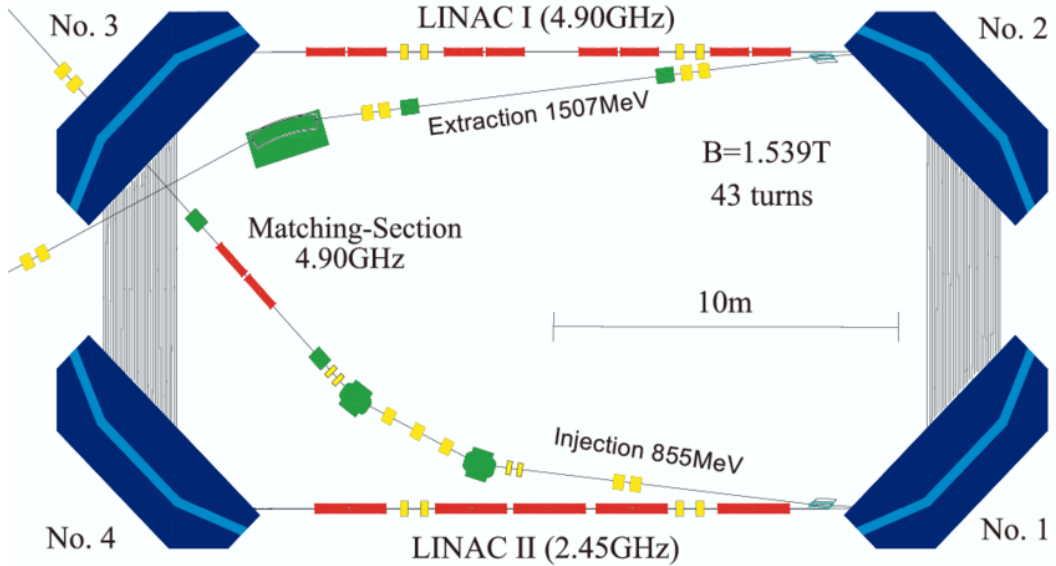


Figure 2.3: The HDSM four bending magnets and the two LINAC sectors allow energies up to 1.5 GeV [18].

- 100 μm diamond, which provides polarized photons through coherent *bremsstrahlung*. Diamond is a crystalline material with a highly ordered microscopic pattern of atoms. Electrons incident upon a crystalline radiator interact with, and transfer momentum to, the crystal as a whole, producing coherent *bremsstrahlung* instead of interacting with single nuclei. The coherent *bremsstrahlung* cross section has a distribution associated with the lattice structure of the crystal. Using the Stonehenge technique [19] it is possible to align the diamond in order to maximize the polarization degree for a given photon energy;
- 10 μm copper, which provides unpolarized photons. Standard copper is made of grains, each of them with lattice structure. Nevertheless, the global distribution results in an amorphous material since the grains are randomly oriented. Electrons incident upon an amorphous radiator produce incoherent *bremsstrahlung* with a typical $\frac{1}{x}$ cross section distribution;
- 10 μm moeller, used only for systematic studies of the photon flux.

During the run period of March 2018, the current of the incident electron beam was 3.5

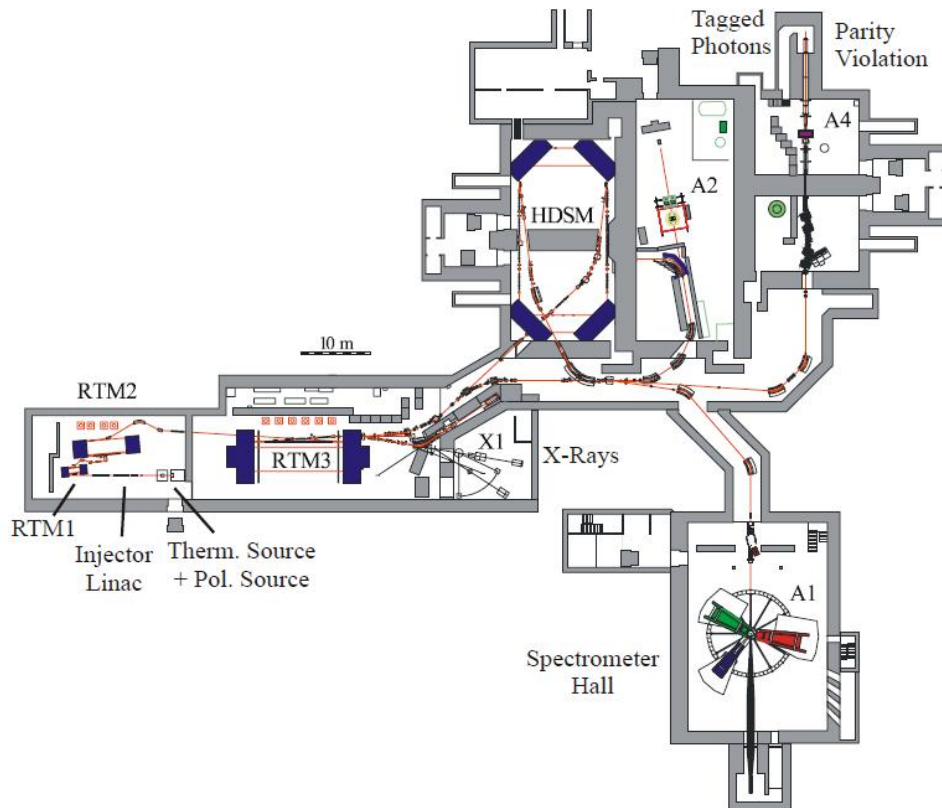


Figure 2.4: The MAMI facility comprises three racetrack microtrons (RTM1, RTM2, RTM3), along with the Harmonic Double Sided Microtron (HDSM), which can accelerate electrons up to 1.5 GeV. Four experimental halls are also depicted (A1, A2, A4, X1) [17].

nA for the diamond radiator and 9 nA for the copper and moeller radiators.

2.3 Glasgow Tagged Photon Spectrometer

The Glasgow Tagged Photon Spectrometer, or Tagger, is a large dipole magnet with a focal plane detector system that allows the momentum analysis of the *bremsstrahlung* electrons.

For an incident electron with initial state (E_0, \mathbf{p}_0) and final state (E, \mathbf{p}), which produces a photon (k, \mathbf{k}) and transfers momentum \mathbf{q} to the nucleus, the conservation of energy and momentum implies:

$$E_0 = E + k, \quad (2.1)$$

$$\mathbf{p}_0 = \mathbf{p} + \mathbf{k} + \mathbf{q}. \quad (2.2)$$

The photon energy, therefore, can be deduced by the electron energies before and after the photon emission according to the formula:

$$k = E_0 - E, \quad (2.3)$$

where the recoil energy of the nucleus is negligible. The process of calculating the photon energy by detecting the *bremsstrahlung* electron is defined as tagging.

A large dipole magnet is needed to bend the electron pathway with a radius of curvature given by

$$r = \frac{p}{qB}, \quad (2.4)$$

where p is the particle momentum, q its electric charge and B the magnetic field provided by the dipole.

Electrons which have not interacted in the radiator are bent by the Tagger's magnetic field into the beam dump, where the electric current I is measured in a Faraday cup. Electrons that radiates through *bremsstrahlung* and thus loose energy are bent by larger angles and they impinge on the Tagger's focal plane detector (FPD) system. The position at which the electrons are detected in the FPD can be used to extract the energy of the *bremsstrahlung* electrons using Equation (2.3).

The tagging process is shown in Figure 2.5. For an electron beam of 883 Mev, a 1.059

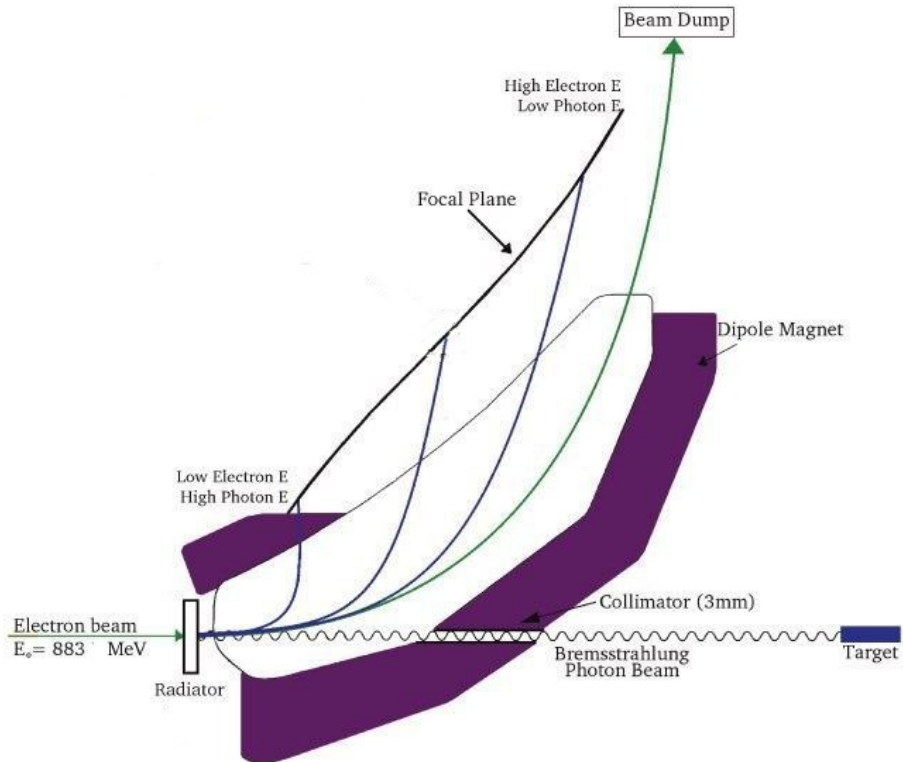


Figure 2.5: The Tagged Photon Spectrometer. Electrons which not interact within the radiator are bent to the beam dump. Electrons that produce *bremsstrahlung* photons are detected by the Tagger's focal plane. Outgoing photons are collimated and continue to the target. The photons energy is inferred by the electrons momentum analysis [17].

T magnetic field was used.

The focal plane detector system consists of an array of 328 Tagger channels of plastic scintillators, each one is roughly 0.6 cm wide, 3 cm long and 0.6 cm thick and coupled to a silicon photomultiplier tube (SiPMT).

A timing coincidence is then used to match the electron signal in the Tagger with the corresponding hits in the reaction-product detectors (CB or TAPS, see Sections 2.5.1, 2.5.2).

The flux of electrons, N_e , is measured with a scaler module that counts the discriminated signals in each Tagger channel. For the calculation of cross sections values, photon flux measures are needed. Due to the collimation of the *bremsstrahlung* photon beam, the photon flux within the target cannot be inferred from the electron flux: dedicated measurements are performed in the tagging efficiency runs (see Section 3.4).

2.4 Liquid hydrogen target

Depending on the experiment, different types of target are available, included a butanol polarized frozen-spin target. During the data-taking of March 2018, the beam of photons impinged upon an unpolarized liquid hydrogen target with $4.248 \cdot 10^{23}$ proton/cm² density. The cylindrical target cell, shown in Figure 2.6, was made of Kapton, 10±1 cm long and 125 μ m thick, and filled with LH₂ at 1080 mb pressure [20]. Additional layers of insulating materials (for example Mylar and Aluminium) were wrapped around the target cell to help keeping the 21 K temperature.



Figure 2.6: The target cell is shown in the inner part of the red structure.

2.5 Detectors

The detector system is composed of the Crystal Ball and TAPS calorimeters, two Multiwire Proportional Chambers and the Particle Identification Detector. Combining the information from all these detectors it is possible to achieve an accurate energy and angular distribution reconstruction and particle identification in the region from 0° to 360° in the azimuthal angle ϕ and approximately from 2° to 160° in the polar angle θ .

2.5.1 Crystal Ball

The Crystal Ball (CB) is a highly segmented electromagnetic calorimeter composed of 672 thallium-doped sodium iodide, NaI(Tl), scintillation crystals. The total energy deposited in the Crystall Ball is used as a trigger condition for the event readout; in March 2018, the trigger threshold was 45 MeV.

As shown in Figure 2.7, each CB crystal is shaped like a truncated pyramid 40.6 cm high (corresponding to 15.7 radiation lengths [21]) pointing towards the centre of the target. The scintillation light goes through a 5 cm air gap and a glass window before reaching a Photo-Multiplier Tube (PMT). The signal is then sent to an analog-to-digital (ADC) converter and finally to a time-to-digital (TDC) converter. The sides of the triangle at the inner and outer surfaces are 5.1 cm and 12.7 cm long respectively. Each crystal is optically isolated from its neighbouring since it is wrapped in thin layers of reflective Mylar foil. The spherical shape of the Crystal Ball is approximated by an icosahedron with an inner radius of 25 cm and an outer radius of 66 cm [22]. The Crystal Ball is split in two hemispheres that can be separated to give access to the central region (target, PID, MWPCs). The CB surrounds the target covering 94% of the 4π solid angle and it lacks of 24 crystals both in the forward and in the backward region in order to not interfere with the photon beam; it covers a polar angle from 21° to 159° and an azimuthal angle of approximately 360° .

The energy loss of photons within the Crystal Ball is mainly due to the pair production which gives rise to electromagnetic showers. Since pair production cross section σ scales with the square of the atomic number Z of the medium (this means that $\sigma \propto Z^2$), the high density and the high atomic number of NaI make it a good inorganic scintillator

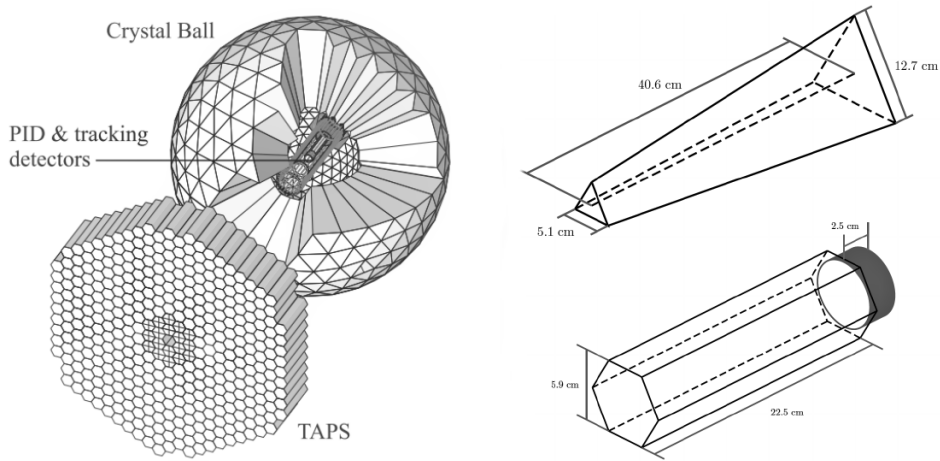


Figure 2.7: On the left side of the picture, CB and TAPS are shown along with the inner detectors in the CB. On the top right and on the bottom right of the picture, a CB truncated pyramid crystal and a TAPS hexagonal prism crystal are presented, respectively, together with their dimensions [23].

material for the detection of the photons. Inorganic scintillators have also a high light output which provides a good energy resolution [24]. Nevertheless, the hygroscopicity of NaI is a big disadvantage that must be taken into account: each hemisphere operates thus only in vacuum. Since the electromagnetic shower produced by photons generally releases energy in more than one crystal, a weighted energy algorithm similar to the center of gravity method is adopted to infer the position of the photon with a good resolution [17]. Resolution for hadrons is not as good as for photons because of the fewer number of crystals involved. The energy resolution provided by the Crystal Ball is 3-4% within the region of interest and, thanks to CB high segmentation, the angular resolution achieved is higher than the crystal size, with values of $\sigma \sim 2\text{-}3^\circ$ in the polar angle θ and $\sigma / \sin \theta$ in the azimuthal angle ϕ [23].

2.5.2 TAPS

While the loss of detection in the backward region of CB is due to the target-related equipment and is, for this reason, inevitable, the forward region not covered by CB is a problem to deal with because of the Lorentz boost of the reaction products.

In order to take care of this problem, the Two Arms Photon Spectrometer (TAPS) is therefore placed 141.7 cm from the target, in front of CB, with the purpose of detecting particles in the downstream polar region with $2^\circ < \theta < 20^\circ$. TAPS presents a small hole where photons with $\theta < 2^\circ$ which have not interacted within the target can pass through.

As shown in Figures 2.1 and 2.7, TAPS is a highly segmented photon calorimeter composed of 366 barium fluoride, BaF₂, crystals and 72 lead tungstate, PbWO₄, crystals. Each BaF₂ crystal has an hexagonal prism shape 22.5 cm long and, together with the others, is ordered in a honeycomb structure to form an hexagonal wall. The PbWO₄ crystals are shaped so that the combination of four of them gives the same shape and size of a BaF₂ single crystal; they form two rings in the innermost part of TAPS improving the angular resolution for events at very small θ angles. Moreover, PbWO₄ crystals offer a better endurance and functioning at high rates. During the run period of March 2018, PbWO₄ crystals were not necessary for the experiment and were switched off. Accordingly, PbWO₄ crystals are not included in this analysis.

TAPS has an angular resolution close to 0.7° and an energy resolution comparable to that of CB [23]. The light output signal of each crystal is collected by a single PMT and then headed to an ADC and a TDC.

TAPS also provides particle identification and particle veto. To accomplish to these tasks, a 5 mm thick and hexagonally shaped scintillator is matched to each BaF₂ crystal and to each group of four PbWO₄ crystals, resulting in a wall of 384 thin plastic scintillators called “Veto wall”. The readout of each scintillator is assigned to a single PMT and their coupling is performed via a wavelenght shifter. The small energy release ΔE in the thin scintillators can be matched to the total energy deposition in TAPS, E, in a two dimensional plot and the particle identification is achieved.

Since the distance between the target and TAPS is greater than the separation between target and CB, it is possible to perform charged particle identification using time-of-flight (TOF) methods. The detection of particles in CB is usually used as a trigger to start the event time $t = t_0 = 0$. The time of a particle detected by TAPS, t_1 , and the energy deposit in TAPS, E, can be ordered into a two dimensional plot so that points are arranged in different regions depending on the mass of a particle.

	Crystal Ball	TAPS
Main spectrometer design	672 NaI(Tl)	366 BaF ₂ and 72 PbWO ₄
Additional detectors	PID, MWPCs	Veto wall
Polar (θ) coverage	21° to 159°	2° to 20°
Azimuthal (ϕ) coverage	0° to 360°	0° to 360°
Polar (θ) resolution	2°	1°
Azimuthal (ϕ) resolution	2°	1°
FWHM γ energy resolution	2%	3%

Table 2.1: Main parameters of the CB and TAPS detectors.

Additionally, the pulse shape analysis (PSA) can be used as a method of particle identification as well. For most scintillators, included BaF₂ crystals, the time evolution of the scintillation light emission process is described by a two-component exponential decay law:

$$N = A \exp\left(\frac{-t}{\tau_f}\right) + B \exp\left(\frac{-t}{\tau_s}\right), \quad (2.5)$$

with a faster τ_f and a slower τ_s decay constants [24]. Depending on the ionizing power, $\Delta E/\Delta x$, of the arriving particle, two distinct states are excited in different proportions, so that their relative intensities change as the particle type changes.

Table 2.1 outlines the main parameters of CB and TAPS.

2.5.3 Particle Identification Detector

The particle path from the target to CB is short because of the small inner radius of CB (25.3 cm) and timing resolution of the Crystal Ball NaI scintillators is not good enough to provide particle identification through time of flight methods. Therefore, an additional detector, the Particle Identification Detector (PID), is needed to allow particle identification of charged particles and to veto electrons in order to clearly identify photons. The PID detector sits within the CB, between the target and the two Multiwire Proportional Chambers even if it is not the most advantageous position: the reaction products get through the PID before reaching the MWPCs and this reduce the resolution

in the tracking of charged particles.

Moreover, its design was tightly constrained by the pre-existing detector geometry. As shown in Figure 2.8, the PID is composed of 24 thin plastic scintillators, each 15 mm x 500 mm x 4 mm, forming a barrel around the target [17]. Each scintillator covers 15° in the azimuthal angle ϕ .

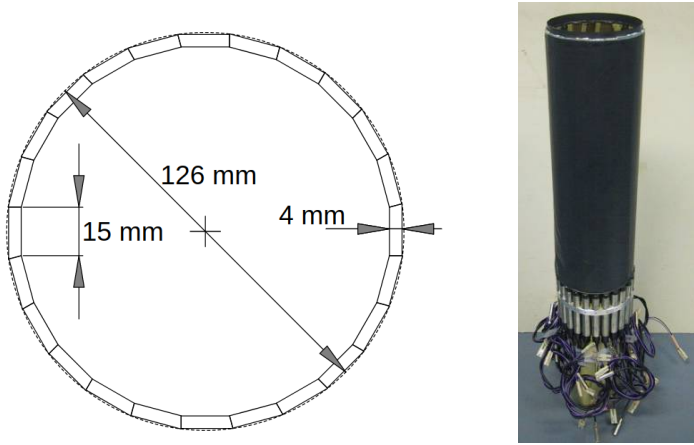


Figure 2.8: The Particle Identification Detector is composed of 24 thin plastic scintillators, each 15 mm x 500 mm x 4 mm, forming a barrel around the target. Each scintillator covers 15° in the azimuthal angle ϕ [25].

The particle identification, as shown in a two dimensional histogram in Figure 2.9, is achieved correlating the particle's differential energy loss ΔE in a thin detector (PID) and the energy E deposited in the calorimeter (CB), which is assumed to be the total energy of the particle. A point in the ΔE vs E plane is associated to each event and clusters of events come up because of the different energy loss of different charged particles, according to the Bethe-Block formula:

$$\frac{dE}{dx} \propto k \frac{z^2}{E}. \quad (2.6)$$

Two dimensional cuts can be applied to identify protons, electrons and charged pions.

2.5.4 Multiwire Proportional Chambers

The Multiwire Proportional Chambers (MWPCs) are two gaseous ionization detectors 2 mm far from each other, surrounding the PID and within CB. Since CB angular resolu-

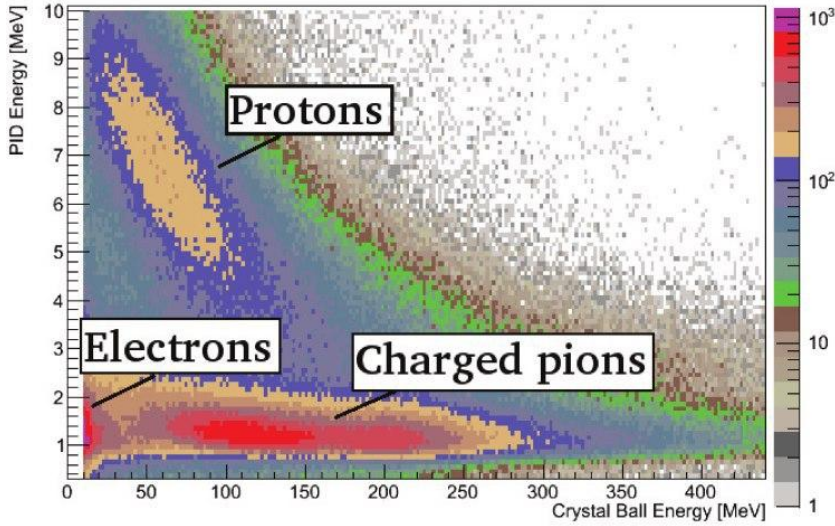


Figure 2.9: An example of the $\Delta E/E$ histogram. For each event is possible to associate a point in the $\Delta E/E$ plane. Clusters of events come up because of the different energy loss of different charged particles [17].

tion for charged particle is not good enough for the A2 experiments because of the small number (1-2) of NaI crystals involved, the MWPCs satisfy the need of a far superior position information.

They have been developed and built by the INFN group in Pavia, using as a prototype the MWPCs of the DAPHNE experiment [26].

Each chamber has a layer of anode wires parallel to the beam direction enclosed in the middle of two layers of cathode strips. The wires have a $20\ \mu\text{m}$ diameter, they are 2 mm far from each other and are made up of tungsten coated with gold. The tension applied to each wire is of 60 g. For each chamber, aluminium strips $0.1\ \mu\text{m}$ thick and 4 mm wide are glued in a spiral geometry to two Rohacell cylinders 1 mm thick and separated by 8 mm. The helical trend of strips in the two cylinders forms a 44.23° angle with respect to the wires disposition and 88.46° with respect to each other.

Figure 2.10(a) depicts the structure of a MWPC; Table 2.2 displays the number of wires, inner strips and outer strips for the innermost and outermost multiwire proportional chamber. In the internal chamber, two different strips cross three times, in the outer chamber they cross twice.

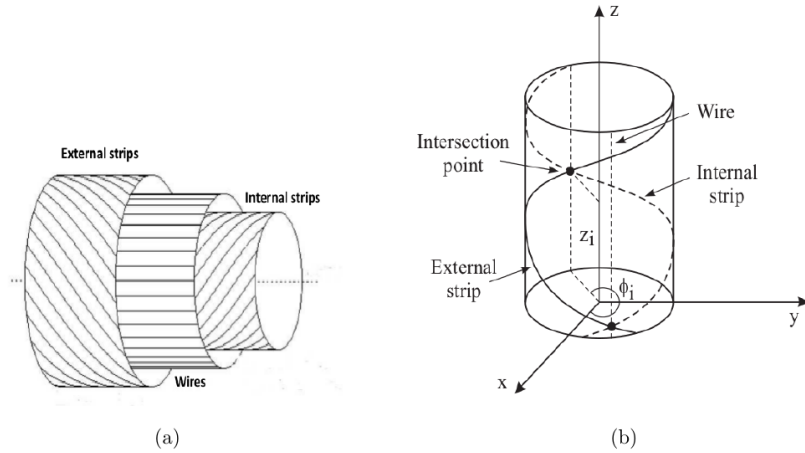


Figure 2.10: (a) A sketch of a MWPC is represented. The MWPC comprises an anode layer of wires between the two cathode layers of strips. Strips are wrapped around two cylinders as helix and they form respect to wires a 44.23° angle and a 88.46° angle respect to the other strips layer [27]. (b) Charged particle hit reconstruction in a MWPC [27].

Inner MWPC	Outer MWPC
No. inner strips	69
No. wires	232
No. outer strips	77

Table 2.2: Number of wires and strips for the two MWPCs.

During the data-taking period, a voltage of 2500 V is applied between anodes and cathodes and the chambers are filled with a specific gas mixture. The gas choice depends on several factors, such as a low working voltage, high gain, good performance at high rates, a good proportionality between MWPC input and output and low costs [24]. The gas used to fill the MWPCs is a mixture of 65.5% Argon, 28% Ethane, 6% Ethanol and 0.5% of Freon.

The passage of a charged particle through the chamber ionizes the gas mixture producing a number of electron-ion pairs (or electron-hole pairs) proportional to the energy deposited by the particle. Because of the electric field induced by the voltage, electrons migrate towards the closer wire (anode) while ions move towards the nearest strip (cathode). As electrons approach to the wire, the electric field becomes much more stronger ($E \propto 1/r$, where r stands for the distance from the wire) giving to electrons energy enough to start second ionization processes and creating an avalanche of electron-ion pairs; keeping the second ionization under control is important to obtain an outgoing signal proportional to the energy deposited within the chamber. The number of electrons is therefore increased to produce a signal big enough to be collected by wires. Furthermore, the ions drifting towards the strips induces a positive signal on the cathode.

As outlined in Figure 2.10(b), the charged particle hit position is inferred by the analysis of wire and strip signal intersections: a single signal from both internal and external strips allows to reconstruct two points $((\phi_{ss1}, z_{ss1})$ and (ϕ_{ss2}, z_{ss2})) using ϕ angle and z coordinate information. It is the signal from the wire that gives the unambiguously value of ϕ to calculate the hit position.

The angular resolution for MWPCs is approximately 2° both in θ and ϕ with efficiency up to 80% for protons at $\theta = 90^\circ$.

Table 2.3 sums up the different methods of charged particle detection used by the PID, MWPCs, Veto wall and TAPS. Table 2.4 below shows the experimental setup and the main parameters of March 2018 beamtime.

PID	$\Delta E/E$ method
2 MWPCs	Tracking
Veto wall	$\Delta E/E$ method
TAPS	Time-of-flight, Pulse shape analysis

Table 2.3: PID, MWPCs, Veto wall and TAPS methods of charged particles detection.

Experimental conditions March 2018
Unpolarized electron beam: energy 883 MeV
Detectors setup: PID, MWPCs, CB, TAPS, Tagger
Target: 10 cm unpolarized LH ₂
Trigger: CB Esum with threshold at 45 MeV
Radiators: 100 μ m diamond or 10 μ m amorphous
Linearly polarized photon beam with diamond radiator
Unpolarized photon beam with amorphous radiators

Table 2.4: Experimental setup and main parameters of March 2018 beamtime.

2.6 Event readout

The trigger condition plays a key role because it would be impossible to record all the events uninterruptedly; consequently, an online selection to discriminate the potentially interesting events must be done.

The Energy Sum trigger condition of the Crystal Ball consists in the sum of all the photomultiplier signals and the evaluation of the total energy deposition into the CB NaI crystals by the use of a discriminator: if the total energy is greater than 45 MeV, the electronic system starts the event readout. For a better timing resolution, two discriminators are used: one with a low threshold and one with a higher one [17]. The aim of the lower threshold is to start the trigger signal and to inhibit the acquisition system for future events, while the high threshold provides the final experimental trigger. The event information are stored only when both the low and the high threshold are passed.

All the detector elements are coupled to photomultiplier tubes (PMTs) whose raw signals, proportional to the energy release of particles, need to be converted into meaningful information. The signal digitalization is performed by the ADC (Analog to Digital Converter) and TDC (Time to Digital Converter) modules, recording energy and timing information respectively.

Since to each activated Tagger channel corresponds an energy value, the analogic signals coming from the Tagger PMTs are not turned into deposited energy, but the signal is splitted in two, one goes to the free-running scalers and the other to the TDC modules. The MWPCs and the PID are supplied with an easier acquisition system because they never contribute to the trigger condition.

The MWPCs wire and strip signals are amplified and sent to ADCs and TDCs respectively, while the PID scintillators deliver the amplified signals to both ADCs and TDCs. The TAPS signals readout is similar to that of CB, with the difference that the pulse-shape analysis requires a partition for the fast and slow decay components. This means that those signals passing the discriminator are split into three parts: one for the timing information and the other two for the detection of the fast and slow components. TAPS could also be used as trigger in addition to CB, but this was not the case for the March 2018 runs.

Chapter 3

Analysis

3.1 $\gamma p \rightarrow \pi^0 p$ cross section calculation

The cross section is one of the most meaningful measurable quantity in particle physics because it represents the quantum mechanical probability that a specific interaction occurs [1]. In contrast to the reaction rate, that depends on the apparatus design as well as on the experimental variables such as the target density, the beam intensity and the detection efficiencies, the cross section is an intrinsic characteristic of the physical process and it is not affected by the particular experimental setup used for the calculation.

Let's consider a photon beam with energy E hitting a target of protons at rest, with a proton density per unit volume ρ_p and a target length Δz . The photon flux Φ_γ is defined as the number of photons N_γ passing through a unit area per unit time. The number of photons N_i interacting within the target is given by:

$$N_i = \sigma N_\gamma \rho_p \Delta z, \quad (3.1)$$

where the fundamental physical parameter is the proportionality constant σ , the cross section of the process. It is measured in barn, $1 \text{ b} = 10^{-24} \text{ cm}^2$, and it has the dimensions of an area.

The cross section is therefore calculated using the following energy-dependent formula:

$$\sigma(E) = \frac{N_i(E)}{N_\gamma(E) \rho_p \Delta z}. \quad (3.2)$$

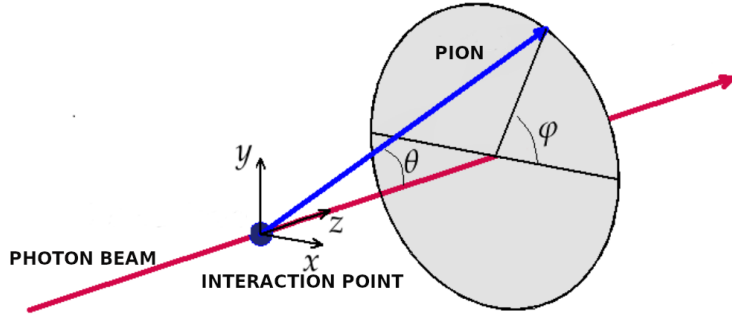


Figure 3.1: The polar and the azimuthal angles, respectively θ and ϕ , of emission of the neutral pion are sketched [15].

In the present work, the π^0 photoproduction total cross section is calculated as:

$$\sigma(E_\gamma) = \frac{N_{\pi^0}(E_\gamma)}{N_\gamma(E_\gamma)} \frac{1}{\rho_p \Delta z} \frac{1}{\epsilon_{rec}}, \quad (3.3)$$

where:

- $N_{\pi^0}(E_\gamma)$ is referred to the number of π^0 reconstructed events as a function of the incoming photon energy;
- $N_\gamma(E_\gamma) = N_e(E_\gamma) \cdot \epsilon_{TaggEff}(E_\gamma)$ is the photon flux, as a function of the photon energy, inferred by the product between the number of electrons detected by the Tagger $N_e(E_\gamma)$ and the tagging efficiency $\epsilon_{TaggEff}(E_\gamma)$. $N_\gamma(E_\gamma)$ defines the fraction of photons that reaches the target compared to the produced one;
- ϵ_{rec} is a correction factor representing the π^0 reconstruction efficiency of both the apparatus and the analysis software;
- $\rho_p \Delta z$ is the surface density of the proton target.

An even more complete information can be obtained by studying the dependency of the cross section on the polar and azimuthal angles, the other independent variables that describe the process. Figure 3.1 sketches θ and ϕ , respectively the polar and the azimuthal angles of emission of the neutral pion.

Considering the number of interacting photons per unit time in the solid angle region

$d\Omega = \sin \theta d\theta d\phi$ for a fixed energy E_γ , it follows that:

$$d\sigma(\theta, \phi) = \frac{dN_i(\theta, \phi)}{N_\gamma} \frac{1}{\rho_p \Delta z}. \quad (3.4)$$

The cross section as a function of the scattering angles is called “differential cross section” and is given by:

$$\frac{d\sigma(\theta, \phi)}{d\Omega} = \frac{dN_i(\theta, \phi)}{d\Omega} \frac{1}{N_\gamma} \frac{1}{\rho_p \Delta z}. \quad (3.5)$$

The total cross section $\sigma(E_\gamma)$ may be resumed by integrating the differential cross section $\frac{d\sigma}{d\Omega}$ over the full solid angle:

$$\sigma = \int \frac{d\sigma(\theta, \phi)}{d\Omega} d\Omega = \int_0^{2\pi} d\phi \int_0^\pi d\theta \sin \theta \frac{d\sigma(\theta, \phi)}{d\Omega}. \quad (3.6)$$

Since the detector system has a finite angular resolution, the full solid angle is necessarily divided into a finite number of finite regions. In the π^0 photoproduction analysis, the $d\sigma(\theta, \phi)/d\Omega$ quantity represents the number of neutral pions reconstructed in the solid angle $\Delta\Omega$. In those angular regions with a small sample of events, $d\Omega$ might be extended in order to achieve a higher statistic and, in this case, the event sum over all the increased $\Delta\Omega$ region is considered ($\Delta\Omega = (\Delta\theta, \Delta\phi)$). The unpolarized and longitudinally polarized π^0 photoproduction cross sections have a cylindrical symmetry around the beam direction and they do not depend on ϕ .

The ϕ independent differential cross section is thus finally given by:

$$\frac{d\sigma(\theta)}{d\Omega} \simeq \frac{1}{\rho_p \Delta z N_\gamma} \frac{1}{2\pi \sin \theta \Delta\theta} \sum_{\theta' \in \Delta\theta} \Delta N_i(\theta'). \quad (3.7)$$

3.2 Software

The software used for a first preliminary analysis is Acqu [28], a C++ analysis framework developed and used by the A2 collaboration in Mainz; it is composed of AcquDAQ for the data acquisition, AcquRoot for a first online monitoring activity, for the offline unpacking of the raw data and for the reconstruction of hits and tracks and, finally, by AcquMC for the Monte Carlo event generation [29]. It is built on the basis of ROOT [30], an object-oriented framework developed at CERN and widely used in experimental nuclear physics. Whenever an event passes the trigger condition, the ADC and the TDC information

are read out and stored by the acquisition program, namely AcquDAQ, for the offline analysis performed by Acqu.

The AcquROOT output (both raw detector hits and reconstructed tracks information) is stored into ROOT trees, an extremely convenient format that stores the information in an event-based format, so that they can be easily retrieved by advancing the index in the tree. This output is then used as input to the GoAT (Generation of Analysis Trees) framework, a C++ based extension of AcquRoot, which provides instruments for particle identification, meson reconstruction and event selection. The output of GoAT is saved into ROOT trees again, in order to give an easy access to the data for further analysis.

3.3 Detector calibration

Each element of each detector must be properly and precisely placed, in order to extract good data. The channel number of the ADCs, TDCs and scalers is never modified, unless some electronic reordering takes place; if the detectors are physically moved with respect to the target, the position parameters must be adapted to the new setup.

The calibration process of most detectors is performed by the software CaLib using a specific AcquROOT class to analyse the calibration parameters. Moreover, all the detectors and the electronic devices need an energy and timing calibration.

3.3.1 Tagger

The energy calibration of the Tagger is not performed by CaLib, but is calculated using the magnetic field value of the tagger dipole used for the specific beamtime.. The calibration is carried out by sending electrons of different energies with a low current to the Tagger. The accuracy of the electron energy provided by MAMI makes this scanning method effective [23]. As shown in Figure 3.2 for an 883 MeV electron beam, this allows to match every Tagger channel to a precise photon energy value. The time calibration of the Tagger makes use of TAPS because of its good time resolution. The time difference between the electron detection in the Tagger and a neutral hit detection in TAPS is plotted as a function of the Tagger channel, as shown in Figure 3.3, and its projection

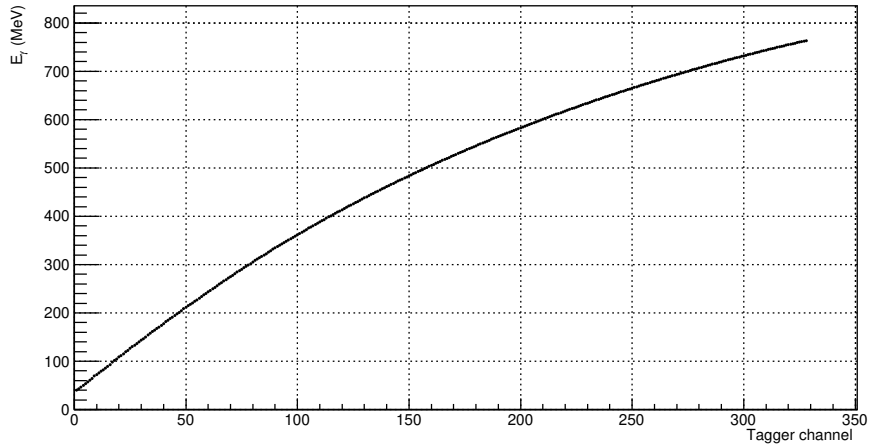


Figure 3.2: Conversion between the Tagger channel and the photon energy value for an 883 MeV electron beam.

on the y axis for each Tagger channel is taken. The peak is fitted with a Gaussian distribution, whose mean must be as close as possible to zero. If it is not close enough, a translational offset equal to the difference between the mean value and zero must be applied to the TDC calibration.

3.3.2 Crystal Ball and TAPS

The Crystal Ball requires a time and an energy calibration, both of them performed with a similar method as that applied to the Tagger time calibration.

As regards the calibration in time, the time difference Δt between two neutral clusters of the same event is plotted as a function of the first NaI hit crystal. For each event, Δt is recorded twice: $\Delta t = t_1 - t_2$ for the first hit crystal and $\Delta t = t_2 - t_1$ for the second hit crystal. The projection over each crystal is then taken and, with a Gaussian fit, the mean of the distribution is calculated. The Gaussian mean should be as much close as possible to zero. If it is not close enough, a translational offset equal to the difference between the mean value and zero must be applied to the TDC calibration. Figure 3.4 shows an example of the 2D plot and its projection over one NaI crystal.

A very preliminary energy calibration of the Crystal Ball is performed using a radioactive $^{241}\text{Am}^{9}\text{Be}$ source with the aim of finding the proper working point of each PMT and

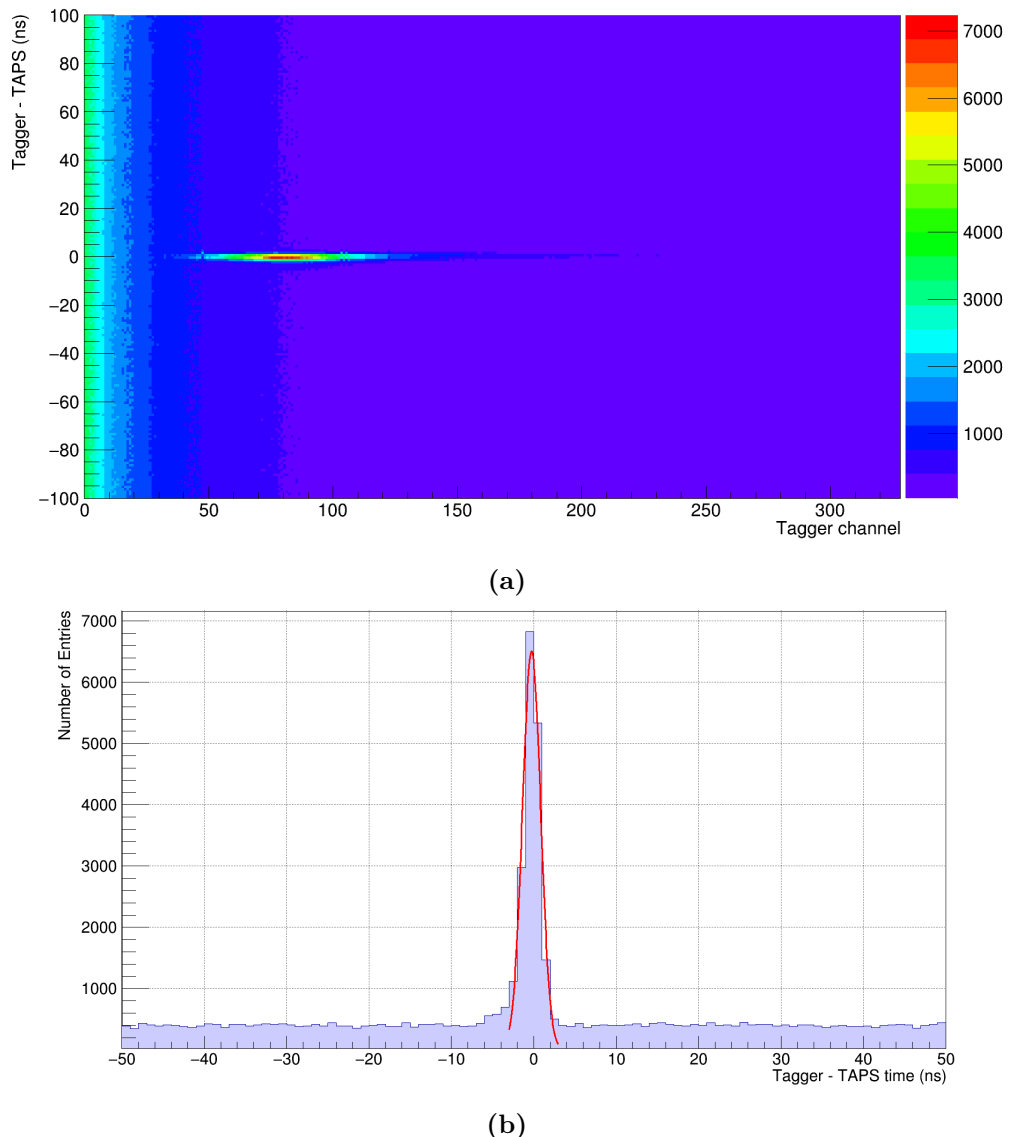


Figure 3.3: (a) Time difference between the electron detection in the Tagger and a neutral hit detected by TAPS as a function of the Tagger channel. (b) y projection of the plot in (a) for one specific Tagger channel, fitted with a Gaussian distribution.

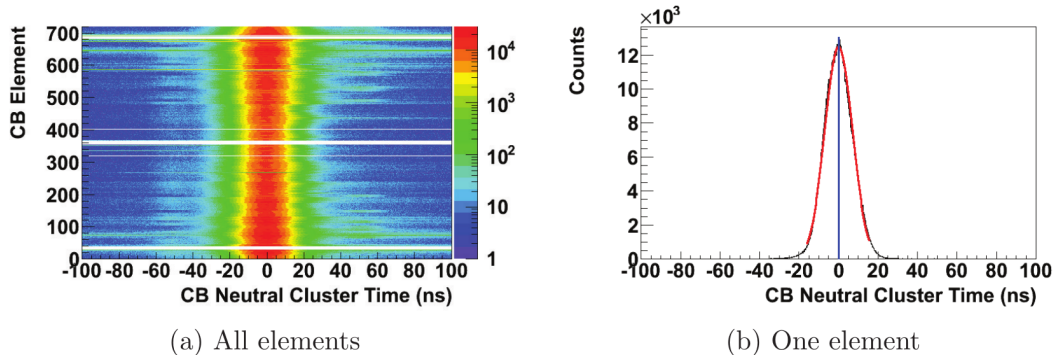


Figure 3.4: (a) An example of the 2D plot representing the time difference Δt between two neutral clusters of the same event as a function of the first NaI hit crystal. (b) The projection over each crystal is then taken and, with a Gaussian fit, the mean of the distribution is calculated[23].

allowing to adjust the voltage supplied to the tube. Then, with an analogous procedure, the energy calibration is carried out: the invariant mass resulting from the two neutral clusters is plotted as a function of the NaI element. Even in this case, the 2D histogram is filled twice for each event, once for each element, with the invariant mass being the same for both of them. The projection over each crystal is considered and the mean of a Gaussian fit distribution has to be peaked on the invariant mass value. If it does not happen, a scale factor to the energy reconstruction must be taken into account.

More complicated calibrations such as the time walk correction and the quadratic energy factor are operated, for detailed information see [23].

The TAPS calibration is similar to the CB one, but long gate ADCs and short gate ADCs are used [23].

3.3.3 PID

The PID requires a ϕ , a time and an energy calibration. A calibration on the ϕ angle prevents errors due to the misplacement (e.g. rotations) of the detector with respect to CB. Tracks within PID and within CB are considered: a 2D histogram is filled with the PID's ϕ respect to CB's ϕ as a function of the PID segment number. The projection over each PID segment is fitted with a Gaussian distribution and its mean value gives the corresponding ϕ for the particular segment.

The time calibration is performed as for the CB. The energy calibration of the PID requires a Monte Carlo simulation and is fully described in [23].

3.4 Tagging efficiency

The cross section calculation requires a precise evaluation of the photon flux, which is the number of photons that reach the target during the data-taking period. It is worthwhile to mention that not all the photons coming from the radiator can reach the target: a significant number of them is absorbed by the 3 mm wide collimator, as shown previously in Figure 2.5. The photon flux $\Phi_\gamma(E_\gamma(i))$ is estimated from the energy-dependent tagging efficiency value $\epsilon(i)$, defined as:

$$\epsilon(i) = \frac{N_{e\gamma}(i)}{N_e(i)}, \quad (3.8)$$

where N_e is the number of electrons detected by the Tagger, $N_{e\gamma}$ is the number of electrons in the Tagger in coincidence with a trigger photon in the Lead Glass detector within an interval of 40 ns and i represents the i -th Tagger channel corresponding to a photon energy $E_\gamma(i)$.

A set of tagging efficiency measurements is performed once a day during dedicated runs, called “tagging efficiency runs”, using a Lead Glass detector (PbGlass detector).

The Lead Glass, 20 cm long, 20 cm wide and 20 cm thick, is placed after TAPS at the end of the photon beam line and it is used as a trigger for the measurements. It comprises more than 20 radiation lengths and provides a high photon detection efficiency (nearly 100%) via the Cherenkov light collection.

When a photon enters the Lead Glass, pair production processes occur, producing e^+e^- pairs that travel faster than the speed of light within the lead: Cherenkov light is thus emitted. The light is turned into an electronic signal by a PMT.

The photon rate in the Lead Glass is around 10 kHz in order to prevent saturation effects and to unambiguously match the electron detected by the Tagger with its *bremsstrahlung* photon. Since the rate is very small, before and after each tagging efficiency run, roughly 10 minutes of background measurements without beam are taken to subtract the unwanted electronic noise in the tagger as well as the background radiation due to possible activation of some parts of the apparatus. This background, in fact, would increase the

counts in the Tagger, namely the denominator of the tagging efficiency in Equation (3.8), artificially decreasing it.

The PbGlass count rate without beam is nearly 70-100 Hz and this low rate makes very unlikely to have a random coincidence with an electron in the Tagger, reason why the numerator of the tagging efficiency is basically not affected by this background radiation. Some parts of the Tagger are activated by the electron beam and this makes more complicated to subtract the background. In fact, the level of activation decreases in time following the well-known exponential formula

$$f(t, i) = A(i) + B(i) \cdot \exp^{-\lambda(i)t}, \quad (3.9)$$

where i is the i -th Tagger channel and λ is the exponential decay constant. To correctly subtract the background contribution one needs then to know exactly which is the background rate at a given time t' . For doing so, the function in Equation (3.9) has been used to fit the time distribution of the counts in each Tagger channel, in order to extract A , B and λ .

Unfortunately, the count rate in the single channel is too small to achieve a good fit result, so the λ has been assumed constant for all the channels (this is a good assumption). So, it is extracted by fitting the rate distribution over time, integrated over all the channels. Then, the obtained value of λ has been fixed in Equation (3.9) and the fit has been repeated for every channel in order to find the parameter $A(i)$ and $B(i)$. This allows a precise calculation of the background rate in the i -th channel at a given time t' . The PbGlass tagging efficiency $\epsilon^{PbG}(sc, i)$, for every channel and every scaler read, is given by

$$\epsilon^{PbG}(sc, i) = \frac{N_{\gamma}^{PbG}(i, sc)}{N_e(i, sc) - N_{Bkg}(i, sc)}, \quad (3.10)$$

where sc is the sc -th scaler read.

A scaler read occurs every 1-2 seconds, and the final tagging efficiency is the average value over all the scaler reads. In Figure 3.5 some examples of tagging efficiencies both for copper and diamond radiators are shown.

When the amorphous radiator (copper) is used, the tagging efficiency is almost constant over the Tagger channels. Instead, the use of the diamond radiator results in a greater tagging efficiency in those Tagger channels whose energy corresponds to the character-

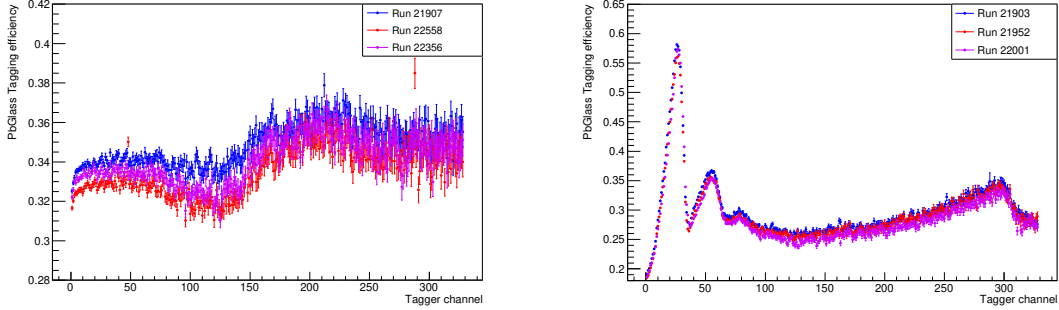


Figure 3.5: Tagging efficiencies for runs with copper radiator (on the left) and with diamond radiator (on the right).

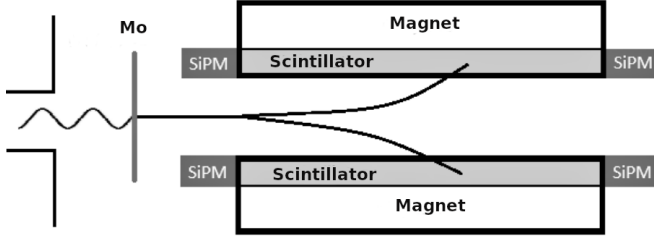


Figure 3.6: A sketch of the Pair Spectrometer. When a photon impinges on the molybdenum (Mo) foil, it is converted with a low probability into a e^+e^- pair. Thanks to the magnets, the e^+ and the e^- are divided in two different paths and are detected by the scintillators [15].

istic energy values of the lattice structure, where coherent *bremsstrahlung* occurs. Even though the tagging efficiency measurements are performed once a day during the data-taking period, the tagging efficiency changes run by run as a consequence of fluctuations of the beam. For this reason, the use of Pair Spectrometer detector allows to apply a correction to the tagging efficiency value for each normal data run.

The Pair Spectrometer (PS) is positioned across the space separating the collimator and the target and, as sketched in Figure 3.6, is composed of two parallel magnets and two parallel scintillators coupled to two silicon photomultipliers (SiPM) each. Ahead of the PS there is a 20 μm thick molybdenum (Mo) foil which converts, with a low probability, photons into e^+e^- pairs. Two 1 T magnets separate the pairs into opposite paths and when the particles impinge on the scintillators, the energy loss is registered by the SiPMs.

When a photon passes through the molybdenum foil, its probability $p(E)$ to convert into e^+e^- pair detected by the scintillators is known as the intrinsic efficiency of the PS. As previously said, this probability has to be low in order to not significantly interfere with the beam and to allow it to operate at high beam rates; on the other hand, a smaller intrinsic efficiency results in a bigger error on the tagging efficiency estimation.

The intrinsic efficiency could be theoretically calculated by the following formula:

$$\epsilon_{theoretical}^{PS}(E) = p(E) = 1 - \frac{\Phi(x)}{\Phi_0} = 1 - \exp[-\mu(E)x], \quad (3.11)$$

where x is the thickness of the molybdenum foil, Φ_0 and $\Phi(x)$ are the photon flux before and after the molybdenum foil respectively. The attenuation coefficient $\mu(E)$ is given by the pair production cross section $\sigma_{e^+e^-}(E)$ and the molybdenum density ρ :

$$\mu(E) = \sigma_{e^+e^-}(E) \frac{\rho N_A}{A}, \quad (3.12)$$

with N_A the Avogadro constant and A the atomic mass. A theoretical approach is however rejected because it would require a precise estimation of the scintillator efficiencies, the geometric efficiency of the detector system, etc.

The Pair Spectrometer intrinsic efficiency is then experimentally extracted during the tagging efficiency runs, when the photon flux is precisely provided by the lead glass, whose efficiency is supposed to be 100%. The intrinsic efficiency is thus defined as the ratio between the number of photons detected by the PS (N^{PS}) and by the PbGlass (N^{PbG}):

$$\epsilon_{intr}^{PS}(i) = \frac{N^{PS}(i)}{N^{PbG}(i)}. \quad (3.13)$$

As shown in Figure 3.7, this method allows to calculate an intrinsic efficiency $\epsilon_{intr}^{PS}(i)$ for each Tagger channel, that can be used in the analysis of the normal runs. The big error bars are due to the low statistics available for one tagging efficiency run.

Since the value of $\epsilon_{intr}^{PS}(i)$ can be considered constant for the duration of a beamtime (~ 3 weeks), in order to increase the statistics it could be convenient to calculate $\bar{\epsilon}_{intr}^{PS}(i)$, i.e. the arithmetic average of $\epsilon_{intr}^{PS}(i)$ over all the tagging efficiency runs. The result is reproduced in Figure 3.8.

The Pair Spectrometer tagging efficiency for each normal run r can be defined as:

$$\epsilon^{PS}(i, r) = \frac{N^{PS}(i, r)}{N_e(i, r)} \frac{1}{\bar{\epsilon}_{intr}^{PS}(i)}, \quad (3.14)$$

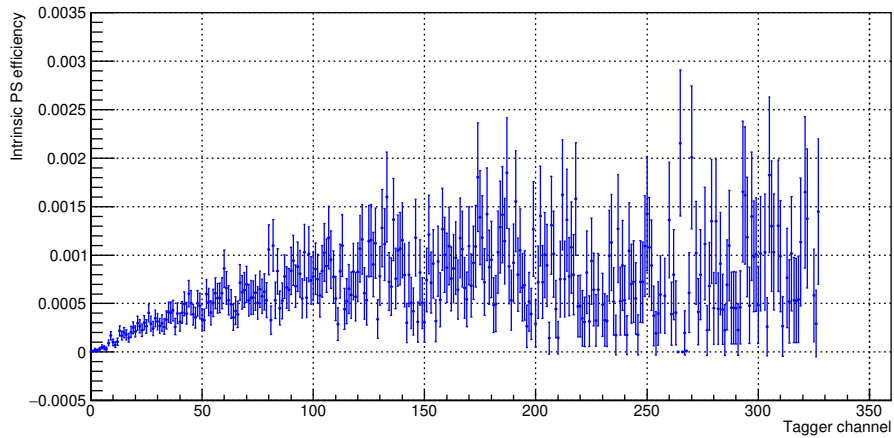


Figure 3.7: The Pair Spectrometer intrinsic efficiency $\epsilon_{intr}^{PS}(i)$ as a function of the Tagger channels for one tagging efficiency run.

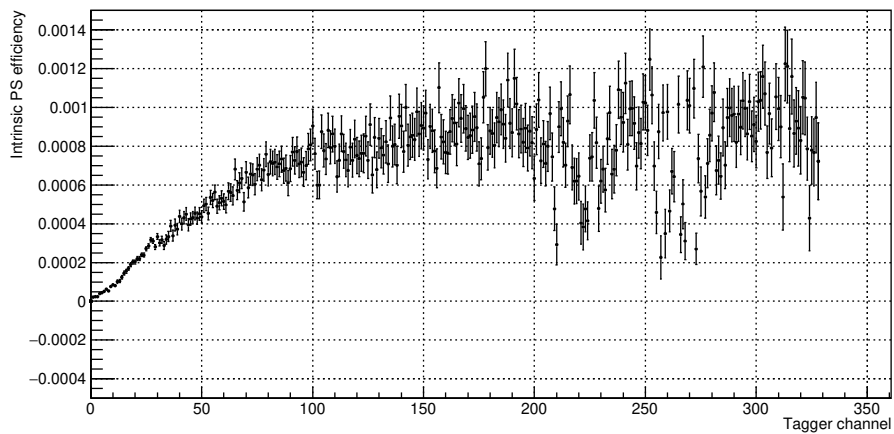


Figure 3.8: The $\bar{\epsilon}_{intr}^{PS}(i)$, i.e. the arithmetic average of $\epsilon_{intr}^{PS}(i)$ over all the tagging efficiency runs, is shown as a function of the Tagger channels.

where $N_e(i, r)$ is the number of electron detected in the i -th tagger channel for the r -th run. The tagging efficiency used in this work for the r -th run is finally given by:

$$\epsilon_{TaggEff}(i, r) = \epsilon_{next-TaggEff-run}^{PbG}(i) \cdot K(r), \quad (3.15)$$

where the overall K scaling factor is given by

$$K(r) = \frac{\bar{\epsilon}_{normal-runs}^{PS}(r)}{\bar{\epsilon}_{next-TaggEff-run}^{PbG}}, \quad (3.16)$$

with

- $\epsilon_{next-TaggEff-run}^{PbG}(i)$: the PbGlass tagging efficiency for the i -th Tagger channel calculated in the tagging efficiency run next in time with respect to the normal run considered;
- $\bar{\epsilon}_{normal-runs}^{PS}(r)$: the PS tagging efficiency averaged over all the Tagger channels for the r -th normal run;
- $\bar{\epsilon}_{next-TaggEff-run}^{PbG}$: the PbGlass tagging efficiency averaged over all the Tagger channels for the tagging efficiency run next in time with respect to the normal run considered.

The tagging efficiency run next in time gives the best estimation of the tagging efficiency value: a MAMI optimization is generally performed once a day after the tagging efficiency runs and since to be optimized is the beam position and the beam spatial spread, the tagging efficiency is significantly affected after this process.

Figure 3.9 simplifies the comprehension of the quantities constituting the K factor: the red triangles represent the $\bar{\epsilon}^{PbG}$ values for the tagging efficiency runs, the black dots depict the $\bar{\epsilon}^{PS}(r)$ values for the normal runs R and the blue triangles stand for the PS tagging efficiency $\bar{\epsilon}^{PS}$ averaged over all the Tagger channels calculated in a tagging efficiency run. This latter value is not used for the $\epsilon_{TaggEff}(i, r)$ estimation, but it is used just as a cross-check for the method. Indeed, in the tagging efficiency runs where we have both the information from the PbGlass and the PS, the two tagging efficiencies calculated with the two methods must be in agreement. Since the tagging efficiency both for the PbGlass and the PS can be slightly different channel by channel depending

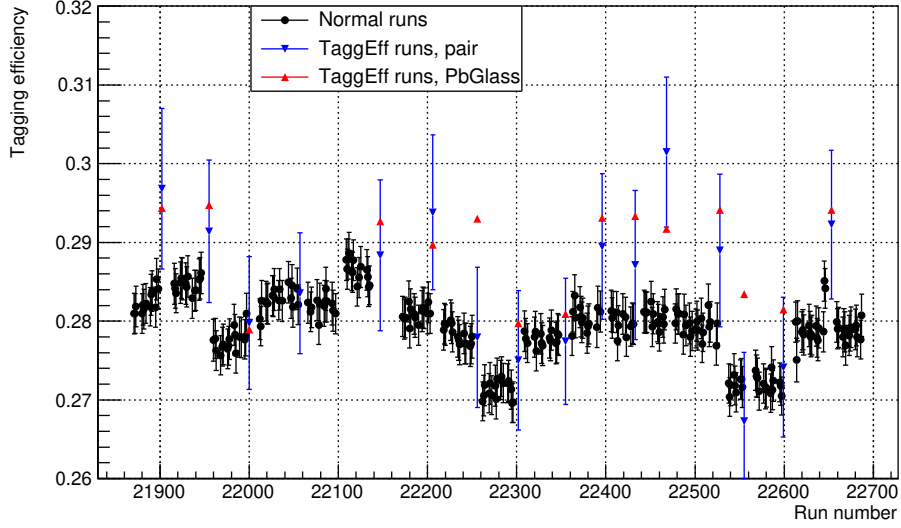


Figure 3.9: Tagging efficiency as a function of the run number: the red triangles represent the $\bar{\epsilon}^{PbG}$ values for the tagging efficiency runs, the black dots depict the $\bar{\epsilon}^{PS}(r)$ values for the normal runs r and the blue triangles stand for the PS tagging efficiency $\bar{\epsilon}^{PS}$ averaged over all the Tagger channels calculated in the tagging efficiency run.

on whether the diamond radiator or the amorphous radiator is used (be reminded the coherent *bremsstrahlung* peak in the diamond radiator case), in the following analysis the tagging efficiency used has been separately calculated for the parallel and perpendicular (or antiparallel) diamond radiator configurations (with polarization planes separated by 90° degrees) and for the amorphous radiator as well.

Equation (3.15) gives a general method for the tagging efficiency calculation for each run and for each Tagger channel.

The photon flux can be finally calculated using the following formula:

$$N_\gamma(i, r) = N_e(i, r) \cdot \epsilon_{TaggEff}(i, r). \quad (3.17)$$

Random	[-300 ns, -30 ns]
Prompt	[-15 ns, +15 ns]
Random	[+30 ns, +550 ns]

Table 3.1: Time cuts applied for the random and prompt regions.

3.5 Event reconstruction

3.5.1 Random event subtraction

The relatively high electron beam of MAMI results in a great number of accidental hits in the Tagger during the time coincidence window opened by the trigger. Among all the *bremssstrahlung* electrons (called randoms), it is therefore necessary to identify the electron (called prompt) that produced the photon that has generated the event.

The prompt electron identification process is performed by computing the time lapse Δt between the incoming $\gamma\gamma$ event registered in CB ($t_{\gamma 1}, t_{\gamma 2}$) and the arrival of the corresponding electron in the Tagger (t_{Tagger}). The time interval Δt for the $\gamma p \rightarrow \pi^0 p$ reaction is calculated with the following formula:

$$\Delta t = t_{Tagger} - t_{CB} = t_{Tagger} - \frac{t_{\gamma 1} + t_{\gamma 2}}{2}. \quad (3.18)$$

Figure 3.10 shows the hit distribution as a function of Δt ; the prompt peak and the two random regions selected with the time cuts in Table 3.1 are depicted. Considering the unwanted background underlying the peak equal to that of the random regions (this is a good assumption, as proved in Figure 3.10), the electrons that accidentally hit the Tagger during the time window opened by the trigger can be removed.

The number of real events is finally given by:

$$N_{true} = N_{prompt} - \frac{\Delta t_{prompt}}{\Delta t_{random}} N_{random}, \quad (3.19)$$

where Δt_{prompt} and Δt_{random} represent the width of the prompt and random time intervals, respectively.

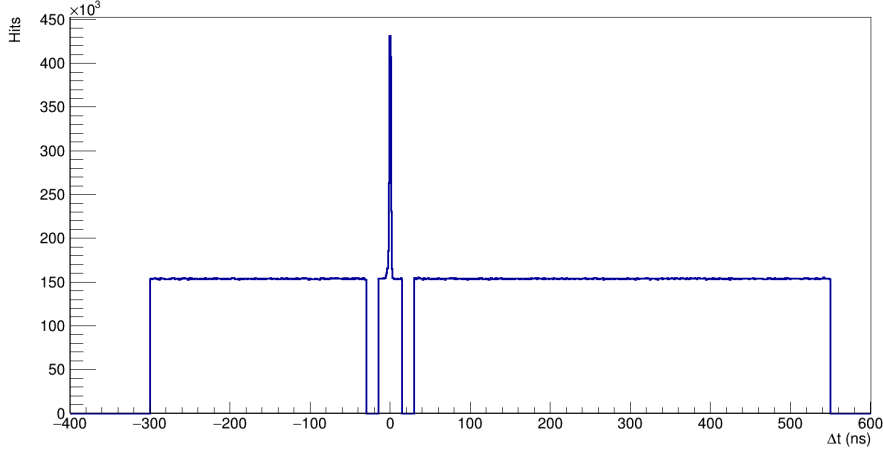


Figure 3.10: Distribution of the time lapse Δt , defined as $t_{Tagger} - t_{CB}$. The prompt peak and the two random regions selected with the time cuts in Table 3.1 are shown.

3.5.2 Livetime

As previously mentioned in Section 2.3, the electron flux is measured with one scaler for each Tagger channel, which counts the discriminated signal. The livetime record of the detector system requires additional scalers. When an event passes the trigger threshold, the data acquisition system is inhibited for the time needed to digitize and record the information. During this time, called “dead time”, the system is not able to store any additional information about other good events and the livetime scalers are inhibited as well. The livetime corresponds to the percentage of time the system remains open to other signals and is defined as the ratio between the time those scalers are inhibited and the functioning time measured by the Tagger scalers.

3.5.3 Event selection for $\gamma p \rightarrow \pi^0 p$ reaction

The mass of the π^0 is of 134.98 MeV and its mean lifetime is $\tau = 8.52 \cdot 10^{-17}$ s. If the pion has an energy of 1300 MeV, its Lorentz factor γ will be

$$\gamma = \frac{E}{m} \simeq 10 \quad (3.20)$$

and it will travel a distance of $x = \gamma\beta c\tau \simeq = 250$ nm, where $\beta \simeq 1$, before it decays into two photons. This distance is definitely too small for the pion to exit the target and

reach any of the detector, so it must be detected by searching for its decay products. The π^0 decays in two photons with a branching ratio of $(98.823 \pm 0.034)\%$ and it decays into $e^+e^-\gamma$ in the $(1.174 \pm 0.035)\%$ of the cases [31]. In the present analysis, only the $\gamma\gamma$ decay mode has been taken into account and the small contribution missing from the other decay channels has been considered within the Monte Carlo efficiency correction. In the center of mass frame, the photons of the $\pi^0 \rightarrow \gamma\gamma$ decay channel are emitted back-to-back along the same direction and the energy of each photon is equal to half of the pion mass. The $\phi_{\gamma\gamma}$ angle between the two photons reaches a maximum value when the product of the photon energies $E_{\gamma 1}E_{\gamma 2}$ is maximum, while $\phi_{\gamma\gamma}$ is minimum when the $E_{\gamma 1} = E_{\gamma 2} = \frac{1}{2}E_{\pi^0}$ condition is fulfilled. Thanks to the high-performance of the A2 equipment in the photon revelation and to the condition that the invariant mass of the two-photon system is close to the pion mass, the π^0 photoproduction can be treated as an almost background-free reaction [17].

The selection applied in this work for the π^0 photoproduction detection in the $\Delta(1232)$ region consists of the following requirements:

- a number $N_{rt} \leq 3$ of raw tracks in the detector system is required. The detection of three raw tracks, $N_{rt} = 3$, corresponds to the detection of one proton and two photons, while the case of $N_{rt} = 2$ considers only the detection of the two photons. In fact, the proton may not reach the Crystal Ball and, in this case, it remains undetected. The other two cases, $N_{rt} = 0$ and $N_{rt} = 1$, are automatically excluded by the next statements;
- a number $N_p \leq 2$ of reconstructed particles is required: exactly one neutral pion and possibly one proton;
- the π^0 has to be reconstructed by using two daughter particles of which, at least one, is a neutral track. This is explained by taking into account the rare (but not negligible) software misidentification of photons: it happens that sometimes GoAT can not properly match track and cluster in the calorimeter (it may happen, for example, when a proton and a photon go through the same PID element) and it labels those tracks as belonging to fictitious particles called “rootinos”, considered as charged particles even if they are not. Figure 3.11 shows the number of rootinos

used for the π^0 reconstruction as a function of the number of reconstructed π^0 . The dashed line indicates the cut applied on the number of rootinos. The events considered in the analysis are the ones on the left hand side of the line. The request of at least one neutral track for the event selection excludes the π^0 reconstruction from more than one rootino, as it would have otherwise happened.

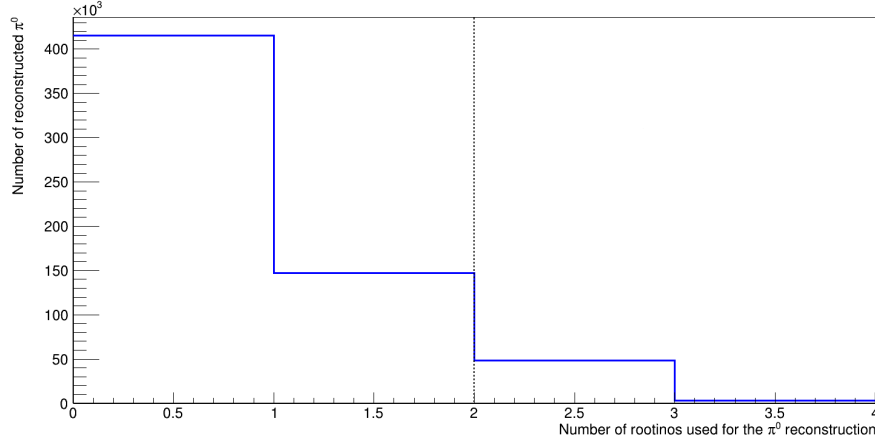


Figure 3.11: The number of rootinos used for the π^0 reconstruction as a function of the number of reconstructed π^0 . The dashed line indicates the cut applied on the number of rootinos. The events considered in the analysis are the one on the left had side of the line.

- after the reconstruction, only the π^0 with an invariant mass in a width of 60 MeV around the nominal π^0 mass have been considered, i.e. $IM = m_{\pi^0} = 134.98 \pm 30.00$ MeV, as shown in Figure 3.12. The finite resolution of the detector system and the stochastic nature of the energy loss process, result in a gaussian distribution of the invariant mass centered on the neutral pion mass (134.98 MeV).

The invariant mass of a particle is the fraction of its total mass independent from its global motion and, in the rest frame of the particle, it is equal to its mass.

Since the neutral pion decays into two photons, the π^0 invariant mass is given by the square root of the sum of the two photon four-momenta:

$$IM = m_{\pi^0} = \sqrt{(p_{\gamma 1} + p_{\gamma 2})^2} = \sqrt{2p_{\gamma 1} \cdot p_{\gamma 2}} = \sqrt{2E_{\gamma 1}E_{\gamma 2}(1 - \cos \phi_{\gamma 1 \gamma 2})}, \quad (3.21)$$

where p_γ is the photon four-momentum and $p_\gamma^2 = p_\gamma \cdot p_\gamma = 0$ because the photon has no mass. $\phi_{\gamma 1 \gamma 2}$ represents the angle between the two photons. For a good

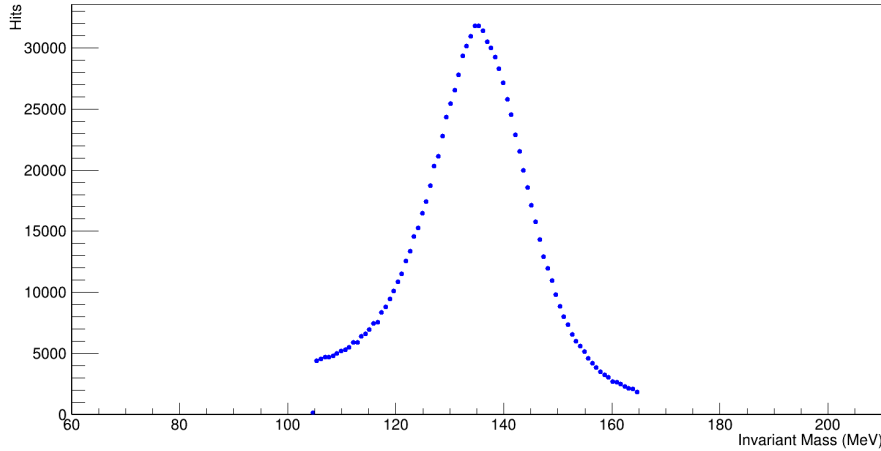


Figure 3.12: Only the π^0 with an invariant mass in a width of 60 MeV around the nominal π^0 mass have been considered, i.e. $IM = m_{\pi^0} = 134.98 \pm 30.00$ MeV.

evaluation of the invariant mass it is therefore necessary both a good angular and energetic resolution. Figure 3.13 shows the invariant mass plots divided into 18 θ bins (θ in the center of mass frame), for a small set of data collected with a full and an empty target. The empty target contribution, correctly normalized, is not negligible and it will be subtracted. For $\theta < 30^\circ$ and $\theta > 160^\circ$ the sample is very small and the invariant mass plots are not well-shaped.

- the energy and momentum conservation laws for the $\gamma p \rightarrow \pi^0 p$ reaction can be written, ignoring the proton that is often undetected, using the four-momenta of the particles as:

$$p_\gamma + p_{proton} = p_{\pi^0} + p_X, \quad (3.22)$$

where the left-hand member considers the photon and the proton four-momenta of the initial state, while the right-hand term comprises the final product of the reaction. The missing four momentum p_X can be found as:

$$p_X = p_\gamma + p_{proton} - p_{\pi^0}, \quad (3.23)$$

and, the missing mass can be then defined as:

$$m_{miss} = (p_\gamma + p_{proton} - p_{\pi^0})^2. \quad (3.24)$$

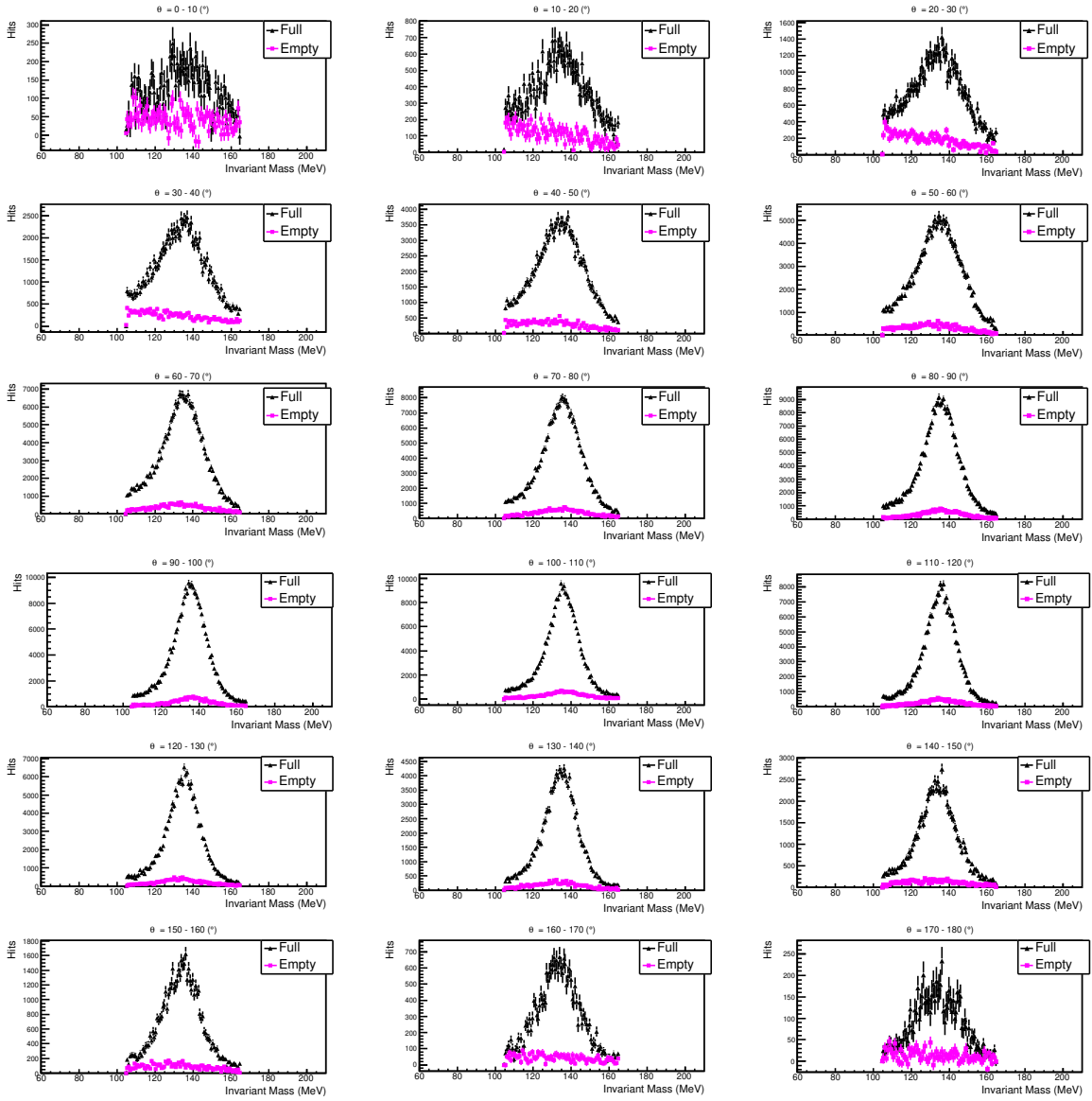


Figure 3.13: The invariant mass plots divided into 18 θ bins, each one covering 10° , for a small set of data collected with a full (black markers) and an empty (magenta markers) target. The empty target contribution, correctly normalized, is not negligible and it will be subtracted. For $\theta < 30^\circ$ and $\theta > 160^\circ$ the sample is very small and the invariant mass plots are not well-shaped.

If the missing particle is actually the recoil proton, then m_{miss} should be equal to the mass of the proton. The finite resolution of the detector system and the stochastic nature of the energy loss process, result in a gaussian distribution of the missing mass centered on the proton mass (938.272 MeV). The missing mass distribution is shown in Figure 3.14. This is taken into account by considering and processing all and only the events with a missing mass value comprised between 850 MeV and 980 MeV, i.e. $MM = [850, 980]$ MeV. It is worthwhile to notice in

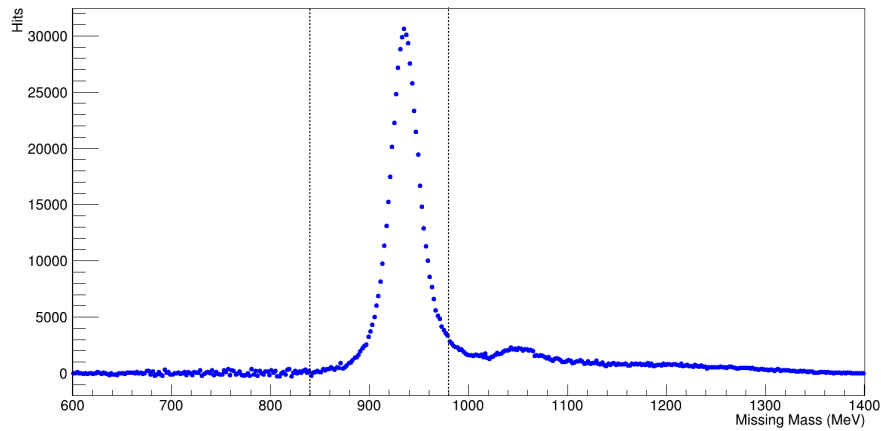


Figure 3.14: The missing mass distribution. All and only the events with a missing mass value comprised between 850 MeV and 980 MeV, i.e. $MM = [850, 980]$ MeV, have been considered. The dashed lines highlight the region within the events have been considered and processed.

Figures 3.12 and 3.14 that to higher values of the missing mass correspond lower values of the invariant mass: this obviously means that an overestimation of the missing mass results in an underestimation of the invariant mass and vice versa. The missing mass plot presents a second small peak around 1050 MeV: the greater number of counts is due to the double pion photoproduction reaction. In this case, the missing mass is the invariant mass of the proton-pion pair. Figure 3.15 shows the missing mass plots divided into 18 θ bins for a small set of data collected with a full and an empty target. The normalized empty target contribution is not negligible and it will be subtracted.

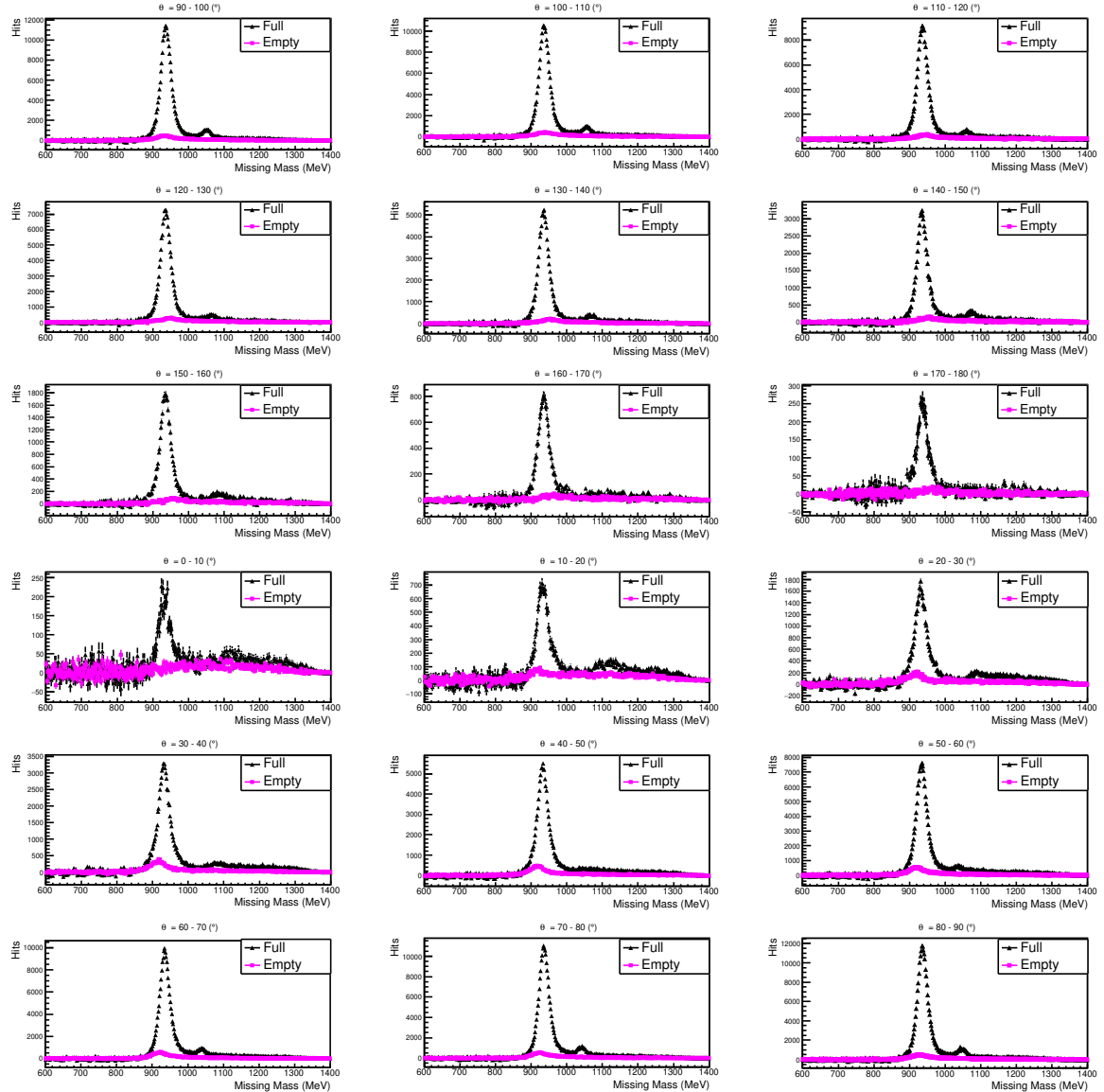


Figure 3.15: The missing mass plots divided into 18 θ bins, each one covering 10° , for a small set of data collected with a full (black markers) and an empty target (magenta markers) are shown. The normalized empty target contribution is not negligible and it will be subtracted.

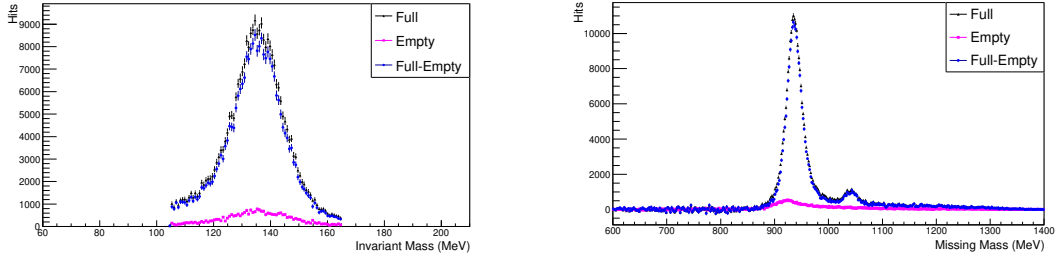


Figure 3.16: Full target (black triangles) and empty target (magenta square) contributions to the invariant mass (left-hand side) and to the missing mass (right-hand side), together with the full contribution with the empty target subtracted (blue dots).

3.6 Empty target subtraction

The target of Liquid Hydrogen, LH_2 , is enclosed in a cylindrical target cell made of Kapton and, around the target cell, additional layers of insulating material are wrapped. The contribution of all the interactions between the incoming photon beam and the target passive materials, except for the Liquid Hydrogen, must be considered and subtracted. During the data-taking period, a few tens of runs with an empty target cell are accomplished with the purpose of evaluating the empty target contribution (N_{empty}). N_{empty} must be normalized in order to ensure an equal incident electron flux for full and empty target data [17]. The empty target contribution normalization is thus calculated:

$$N_{empty} = \frac{\phi_e^{full} \cdot T^{full}}{\phi_e^{empty} \cdot T^{empty}}, \quad (3.25)$$

where ϕ_e^{full} and ϕ_e^{empty} are the incident electron flux for full and empty target respectively while T^{full} and T^{empty} are the livetimes for the full and empty target runs. Figure 3.16 shows the full (black triangles) and the empty (magenta square) target contributions to the invariant mass and to the missing mass, together with the full contribution with the empty target subtracted (blue dots).

3.7 Geant4 π^0 reconstruction efficiency

The errors made in the number of events evaluation are not only limited to the Poissonian uncertainties on the number of counts, but it is also necessary to deal with the

systematic errors related to the equipment and the software. For this reason, an accurate data analysis has to consider a correction factor, namely the event reconstruction efficiency.

In this work, the reconstruction efficiency value takes into account the following systematic biases:

- Geometric efficiency of the detector system. Some angular regions are not covered by any detector: be reminded the backward region of CB, the turned off PbWO₄ crystals of TAPS and the small gap between CB and TAPS. Additionally, the detector system includes a lot of passive elements that contribute to the particle energy loss;
- Intrinsic efficiency of all the different detectors. Every detector has its characteristic intrinsic efficiency lower than 100% that changes for different particles;
- The analysis software efficiency. The offline analysis performed with Acqu and GoAT relies on probability distributions (e.g. invariant mass and missing mass distributions) and is influenced by cuts on some physical quantities (e.g. missing mass cut and time cuts). This may result in event reconstruction errors.

All these factors are taken into account using a Monte Carlo simulation of the $\gamma p \rightarrow \pi^0 p$ reaction.

The correction factor to the total inclusive cross section gives a very small contribution (a few percent) and it has been ignored as a first approximation.

Regarding the π^0 photoproduction, two millions $\pi^0 p$ events are generated using AcquMC; the tracks and hits simulation are processed by A2Geant4 [32], a Monte Carlo simulation software, specifically designed for the A2 collaboration. It is based on Geant4 [33, 34] (GEometry ANd Tracking), an opensource toolkit widely used in nuclear physics intended for the simulation of the passage of particle through matter. A2Geant4 provides a detailed model of the LH₂ target and of the CB-TAPS geometry and functioning, as well as physical models for the electromagnetic and hadronic interactions. The output of the simulation is then analyzed using AcquRoot and GoAT, under the same conditions as for the real data.

The reliability of the simulation has been checked by comparing the missing mass and

the invariant mass plots with those coming from A2Geant4, presented in Figures 3.17 and 3.18; they are divided into 18 θ bins, each one covering 10° , and are depicted both for the data (where the empty target contribution, correctly normalized, has been subtracted to the full one) and for the simulation. As it can be seen, the data distribution reproduces the Monte Carlo simulation results fairly well and the agreement between the two samples is good. The data sample is therefore background-free.

The Monte Carlo reconstruction efficiency value $\epsilon_{rec}(E_\gamma, \theta)$ is then given by the ratio of the number of simulated events reconstructed by GoAT, $N_{rec}(E_\gamma, \theta)$, to the total number of generated events, $N_{gen}(E_\gamma, \theta)$:

$$\epsilon_{rec}(E_\gamma, \theta) = \frac{N_{rec}(E_\gamma, \theta)}{N_{gen}(E_\gamma, \theta)}. \quad (3.26)$$

Figure 3.19 shows the Geant4 Monte Carlo reconstruction efficiency ϵ_{rec} as a function of the θ angle and the Tagger channels (i.e of E). The central region covered by CB has a higher efficiency than the forward and the backward regions.

3.8 Total inclusive cross section

The total inclusive cross section provides the most basic information on the interaction probability. Starting from the initial γp state, it takes into account every possible final states:



where X represents any hadronic final state. Since the total inclusive cross section simply expresses the interaction probability between proton and γ , it does not require any offline selection: any event with a total energy release in the Crystal Ball beyond the 45 MeV trigger condition is accepted and processed. The only corrections needed are the random event subtraction and the livetime. The Geant4 reconstruction efficiency can be ignored as a first-order approximation: its contribution is of 1-2% only.

The total inclusive cross section shares with the π^0 photoproduction some crucial physical quantities as the livetime, the photon flux and, most important, the tagging efficiency. For this reason, the study of the total inclusive reaction provides some meaningful checks on the analysis accuracy.

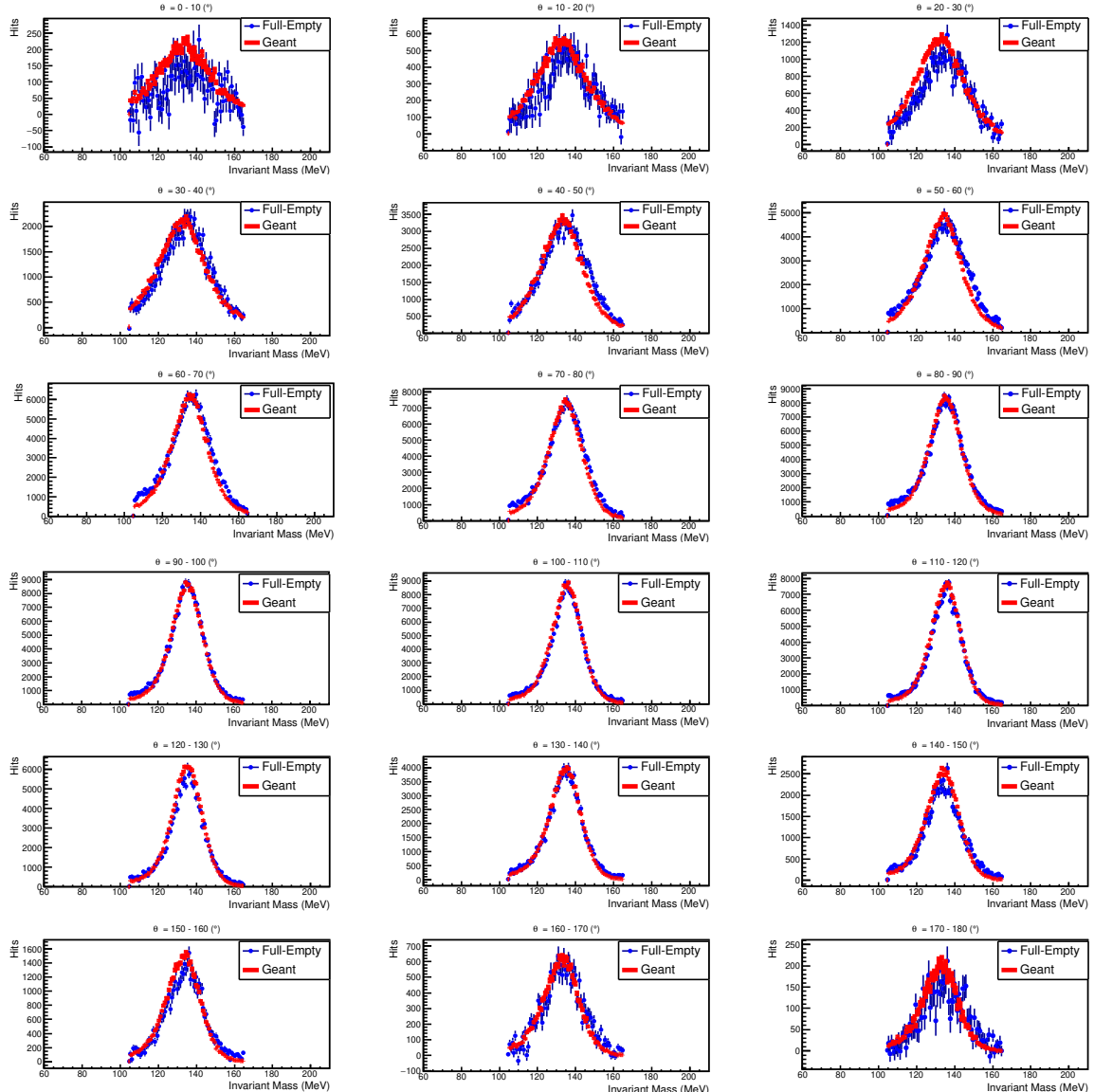


Figure 3.17: The invariant mass distribution is divided into 18 θ bins, each one covering 10° , both for the data (the empty target contribution, correctly normalized, has been subtracted to the full one), in blue, and for the Geant4 simulation, in red.

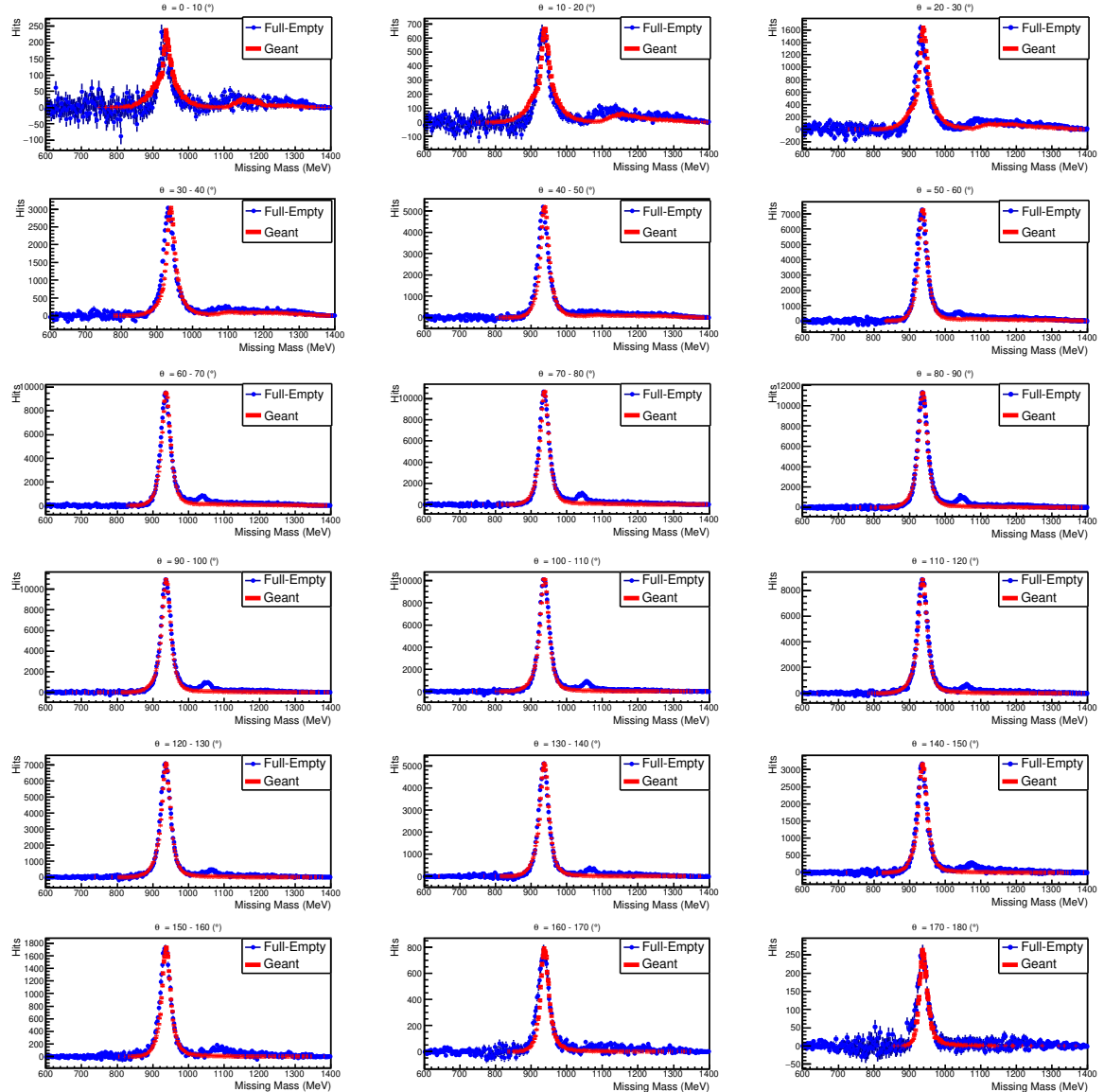


Figure 3.18: The missing mass distribution is divided into 18 θ bins, each one covering 10° , both for the data (the empty target contribution, correctly normalized, has been subtracted to the full one), in blue, and for the Geant4 simulation, in red.

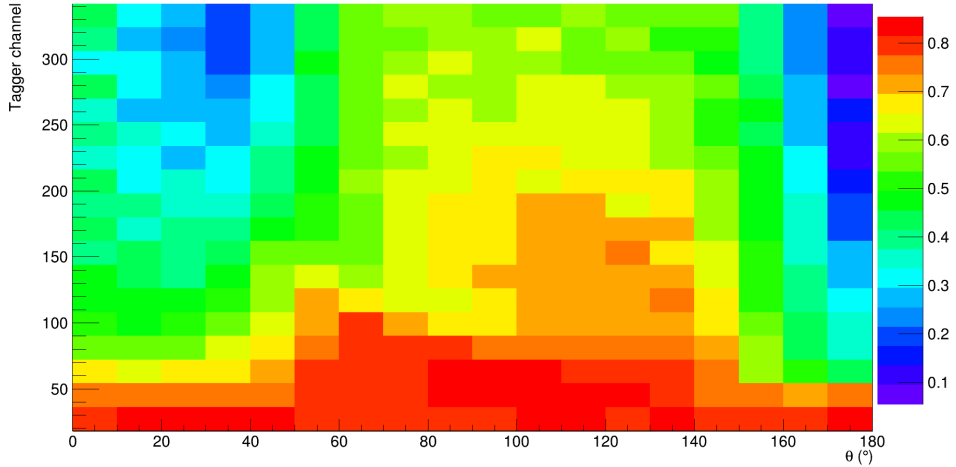


Figure 3.19: The Geant4 Monte Carlo reconstruction efficiency $\epsilon_{rec}(E_\gamma, \theta)$ is plotted as a function of the θ angle and the Tagger channel.

Figures 3.20 and 3.21 exhibit the total inclusive cross sections obtained with an unpolarized photon beam (copper radiator) and with a linearly polarized photon beam (diamond radiator), respectively. The experimental data (blue dots) are compared to the MacCormick et al. [35] analysis (red triangles) carried out with the same experimental conditions. The resonant structure is correctly replicated, as well as the $\Delta(1232)$ main resonance. When the amorphous radiator is used, the data agreement in the $\Delta(1232)$ peak region with the MacCormick et al. results is within 1%, as the linear fit parameter p_0 demonstrates. However, when the crystalline radiator is used, the agreement is within 4% in the peak region. The tagging efficiency is responsible for the difference between the two results, since it is the only different quantity involved. This suggests that additional efforts should be made to achieve a more precise tagging efficiency calculation when one works with the crystalline radiator.

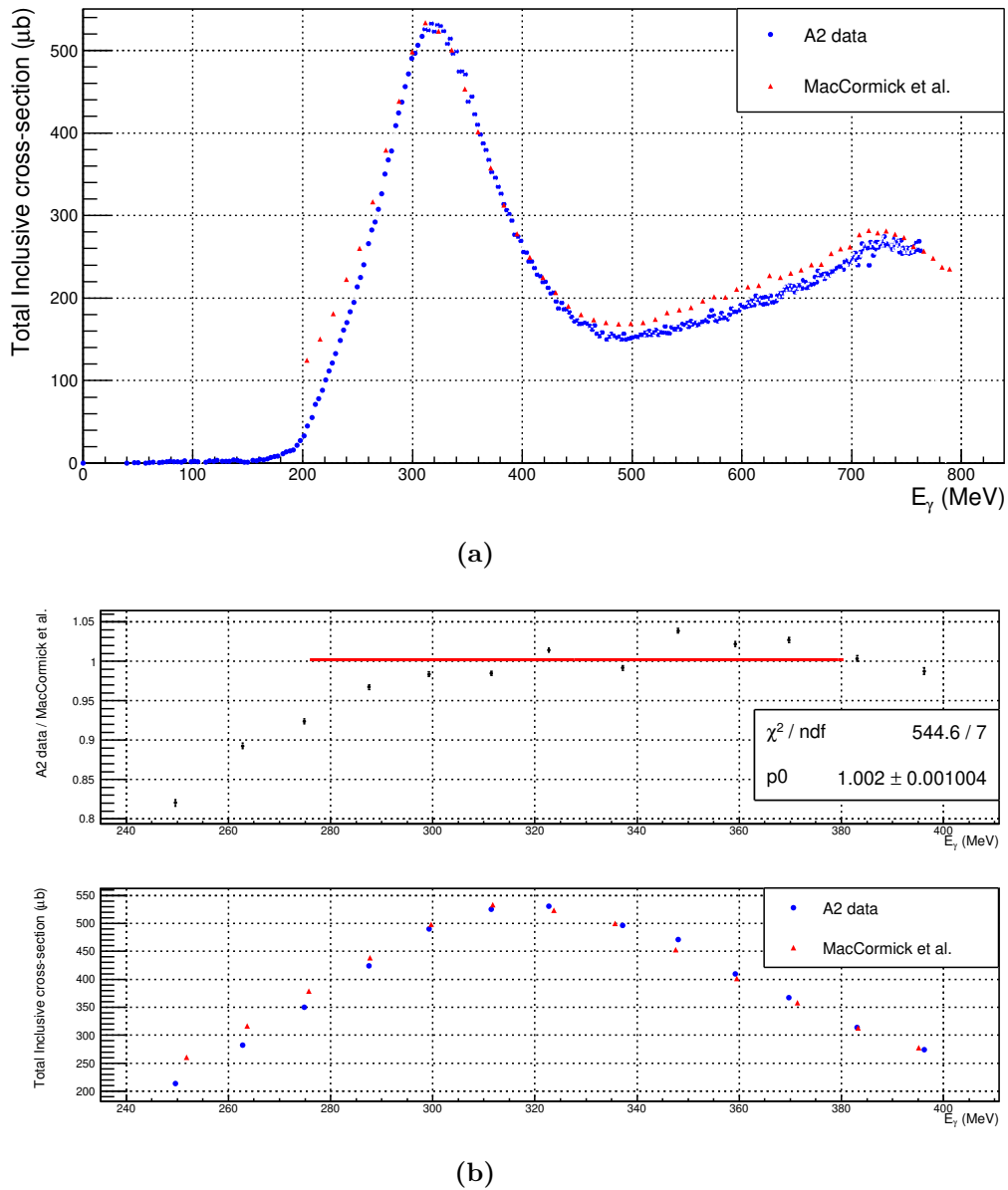


Figure 3.20: The total inclusive cross section obtained with an unpolarized photon beam (a); it is compared with the MacCormick et al. [35] analysis carried out with the same experimental conditions (b).

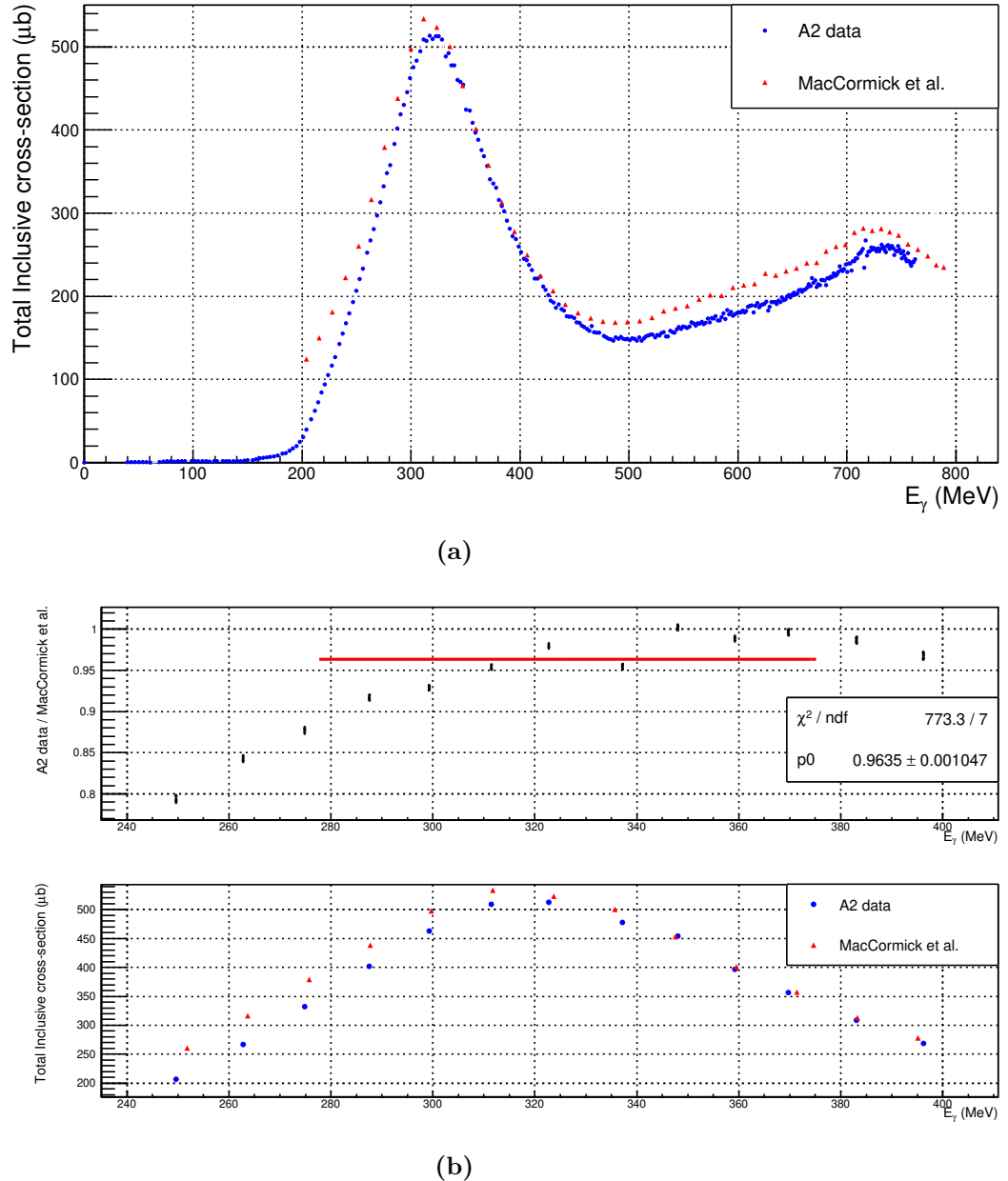


Figure 3.21: The total inclusive cross section obtained with a linearly polarized photon beam (a); it is compared with the MacCormick et al. [35] analysis carried out with the same experimental conditions (b).

Chapter 4

Results

The analysis results of the $\gamma p \rightarrow \pi^0 p$ unpolarized total and differential cross sections, obtained from the data collected in March 2018 by the A2 collaboration (experimental conditions in Table 2.4), are presented in this Chapter.

In addition, the parallel and antiparallel spin configurations of the cross section have been calculated using the polarized cross section, extracted from a different measurement performed by the A2 collaboration in May 2014. Furthermore, the electric quadrupole to the magnetic dipole transition ratio, $R_{EM} = E2/M1$, has been estimated.

4.1 $\gamma p \rightarrow \pi^0 p$ unpolarized cross section

The total unpolarized cross section $\sigma_{\pi^0}^{unpol}$ for the $\gamma p \rightarrow \pi^0 p$ reaction is shown in Figure 4.1 (blue points) both for an unpolarized (a) and a linearly polarized photon beam (b) obtained with the copper and the diamond radiators respectively.

In the $\Delta(1232)$ resonance region, the experimental points match generally well the MAID2007 model predictions [36]. In the energy region above the Δ resonance (350-650 MeV), the MAID2007 model underestimates the cross section but, between 650 and 750 MeV, where the cross section starts to rise again due to the double pion photoproduction, the model correctly reproduces the data.

Figures 4.2 and 4.3 show the differential unpolarized cross section $d\sigma^{unpol}/d\Omega(E_\gamma)$ for different photon energies for an unpolarized and a polarized photon beam obtained with

the copper and the diamond radiators respectively. The errors shown in the plots are only statistical and the error bars are sometimes not visible because of the great statistics available. The experimental blue points are compared to the predictions of the MAID2007 model (red lines).

The agreement between the two distributions is fairly good.

4.2 $\gamma p \rightarrow \pi^0 p$ polarized cross section

In May 2014, the A2 collaboration carried out a series of measurements dedicated to the study of the Compton scattering reaction $\gamma p \rightarrow \gamma' p'$. A circularly polarized photon beam impinging on a polarized butanol frozen-spin target was used.

The running conditions are presented in Table 4.1.

Experimental conditions May 2014
Longitudinally polarized electron beam: energy 450 MeV
Detectors setup: PID, MWPCs, CB, TAPS, Tagger
Target: polarized butanol (C_6H_9OH)
Trigger: CB Esum with threshold at 40 MeV
Radiators: 10 μ m amorphous
Circularly polarized photon beam (i.e. right or left handed, $P_\odot^\gamma = \pm 1$)

Table 4.1: Experimental setup and main parameters of May 2014 beamtime.

A detailed analysis on the main Compton scattering background reaction, i.e. the pion photoproduction $\gamma p \rightarrow \pi^0 p' \rightarrow \gamma' \gamma' p'$, was necessary [37]. The May 2014 data have been analyzed within the A2 collaboration (Prof. P. Pedroni) and the results of the differential $\gamma p \rightarrow \pi^0 p$ polarized cross section, $d\sigma^{pol}/d\Omega(E_\gamma)$, are here used, along with $d\sigma^{unpol}/d\Omega(E_\gamma)$, to extract the parallel and antiparallel cross sections separately ($d\sigma_P/d\Omega(E_\gamma)$ and $d\sigma_A/d\Omega(E_\gamma)$).

The polarized differential cross section $d\sigma^{pol}/d\Omega(E_\gamma)$ for the $\pi^0 p$ channel is obtained as

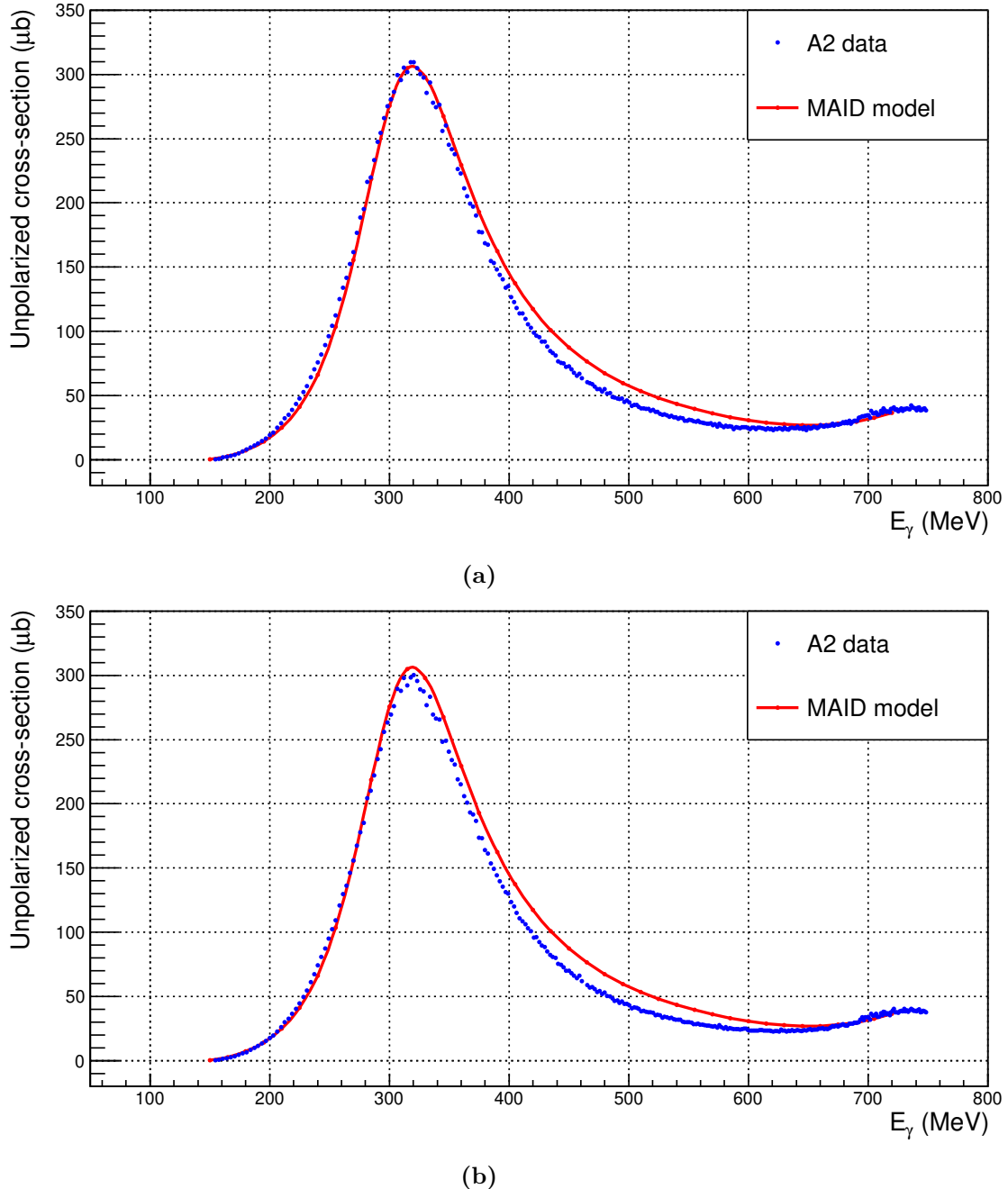


Figure 4.1: Total unpolarized cross section $\sigma_{\pi^0}^{unpol}$ for the $\gamma p \rightarrow \pi^0 p$ reaction measured both with an unpolarized (a) and a polarized (b) photon beam obtained via *bremssstrahlung* on a copper and a diamond radiator, respectively. The red lines represent the MAID2007 cross section prediction. The errors are only statistical and the bars are included into the marker because of the great statistic available.

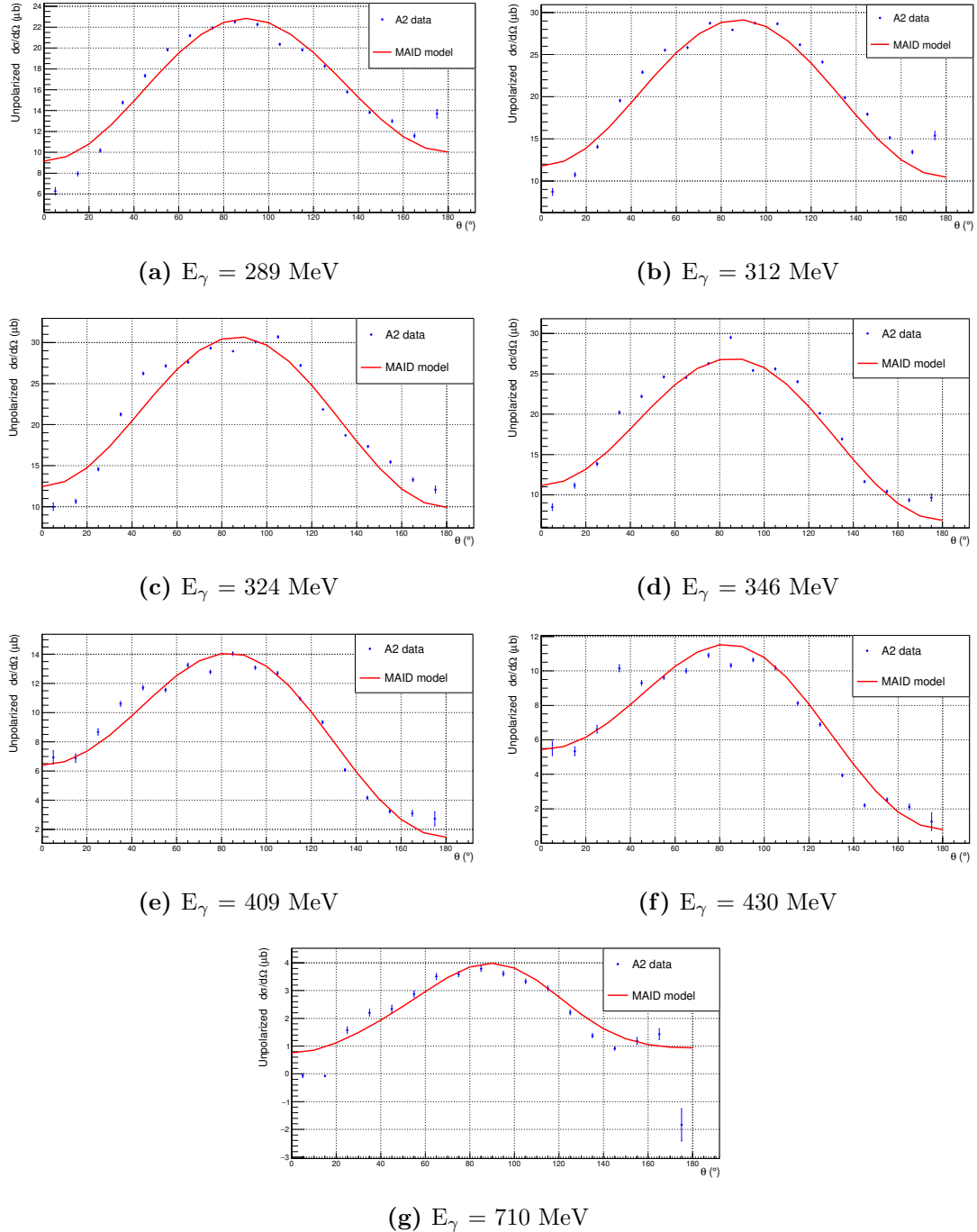


Figure 4.2: Differential unpolarized cross section $d\sigma^{unpol}/d\Omega(E_\gamma)$ for the $\gamma p \rightarrow \pi^0 p$ reaction measured with an unpolarized photon beam for several energies. The red lines represent the MAID2007 model cross section prediction.

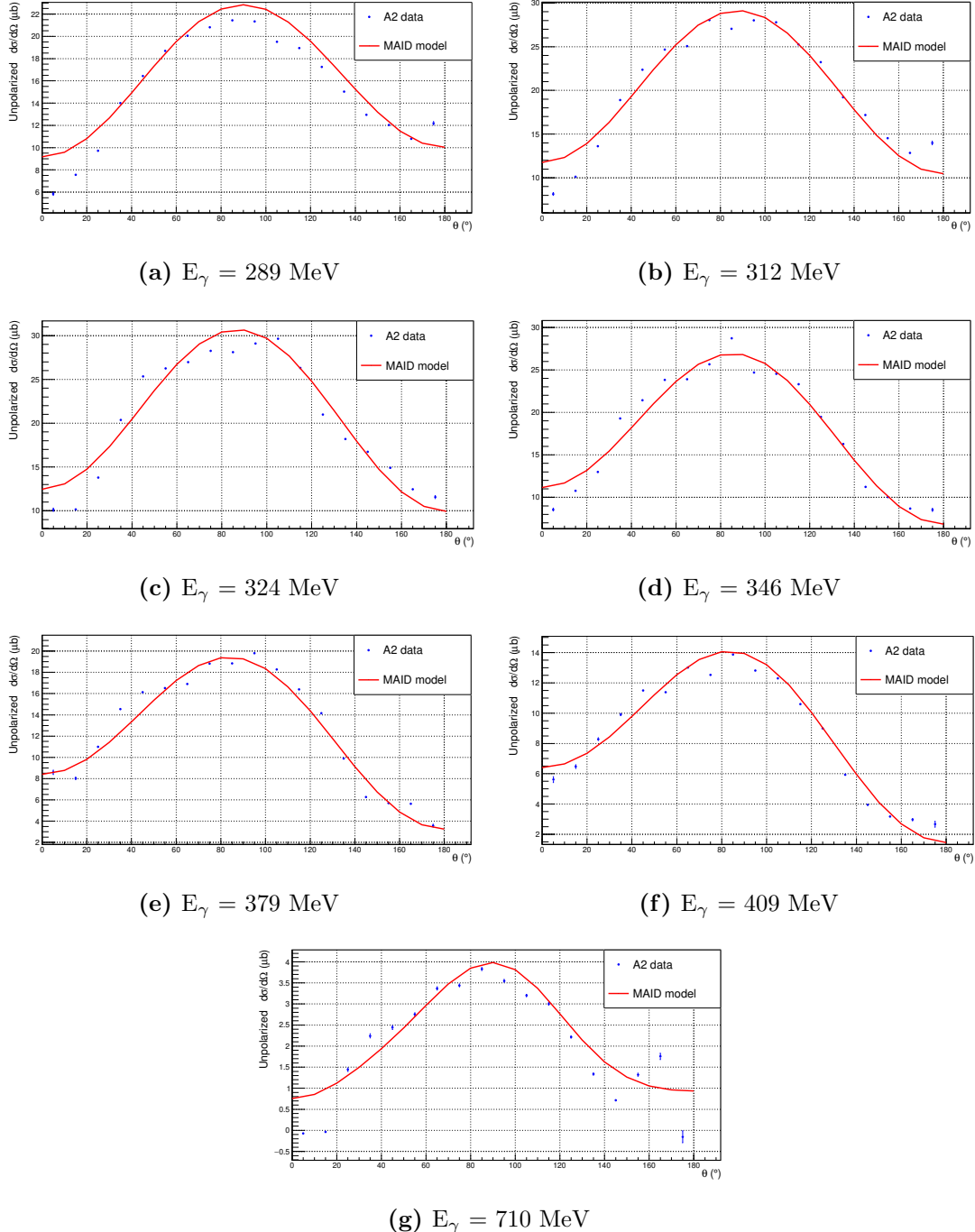


Figure 4.3: Differential unpolarized cross section $d\sigma^{unpol}/d\Omega(E_\gamma)$ for the $\gamma p \rightarrow \pi^0 p$ reaction measured with a linearly polarized photon beam for several energies. The red lines represent the MAID2007 model cross section prediction.

the difference between the helicity-dependent cross sections $d\sigma_P/d\Omega(E_\gamma)$ and $d\sigma_A/d\Omega(E_\gamma)$:

$$\frac{d\sigma^{pol}}{d\Omega} = \frac{d\sigma_P}{d\Omega} - \frac{d\sigma_A}{d\Omega} = \frac{d\sigma_{3/2}}{d\Omega} - \frac{d\sigma_{1/2}}{d\Omega}. \quad (4.1)$$

The subscripts P and A indicate the relative spin orientation between the incident photon and the target proton, parallel and antiparallel respectively. The experimental results for the polarized cross section for the $\gamma p \rightarrow \pi^0 p$ reaction are shown in Figure 4.4. Only eight energy bins around the $\Delta(1232)$ resonance peak, for photon energies from 264 MeV to 399 MeV, are displayed. The data points are compared to the MAID2007 predictions, with a good agreement.

Since the unpolarized cross section for a given energy value can be defined as

$$\frac{d\sigma^{unpol}}{d\Omega} = \frac{1}{2} \left(\frac{d\sigma_P}{d\Omega} + \frac{d\sigma_A}{d\Omega} \right), \quad (4.2)$$

using Equation (4.1) it is possible to extract the separate contributions of σ_P and σ_A , with the following formulas:

$$\frac{d\sigma_P}{d\Omega} = \frac{d\sigma^{unpol}}{d\Omega} + \frac{1}{2} \frac{d\sigma^{pol}}{d\Omega}, \quad \frac{d\sigma_A}{d\Omega} = \frac{d\sigma^{unpol}}{d\Omega} - \frac{1}{2} \frac{d\sigma^{pol}}{d\Omega}. \quad (4.3)$$

The unpolarized cross section information used hereafter for the σ_P and σ_A calculation comes from the linearly polarized photon beam dataset obtained via *bremsstrahlung* on a diamond radiator.

Figures 4.5 and 4.6 show respectively the differential polarized cross section $d\sigma_P/d\Omega(E_\gamma)$ (blue markers) and $d\sigma_A/d\Omega(E_\gamma)$ (red markers) for twelve energy bins, with photon energies from 251 MeV to 399 MeV. The data are compared to the MAID2007 model prediction (black lines) with a fairly good agreement.

4.3 $p - \Delta(1232)$ transition

The gamma quanta can be sort by studying their electric and magnetic multipoles. The electric dipole (E1), quadrupole (E2), octupole (E3), etc, and the magnetic dipole (M1), quadrupole (M2), etc, have a characteristic angular momentum. For example, to the E2 electric quadrupole photon belongs an angular momentum of $l = 2$ in \hbar units and to the M1 magnetic dipole photon an angular momentum of $l = 1$. The angular

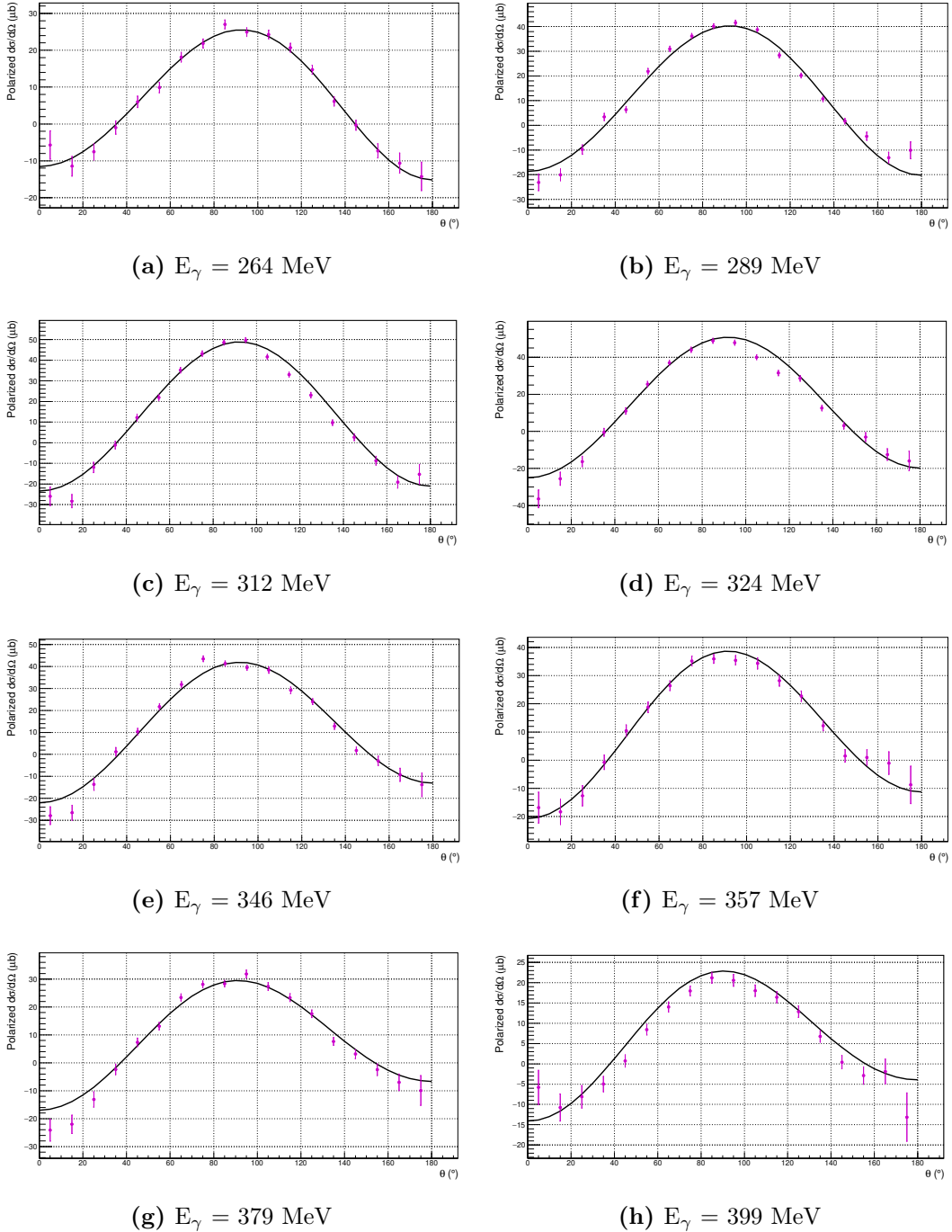


Figure 4.4: Differential polarized cross section for the $\gamma p \rightarrow \pi^0 p$ reaction for photon energies from 264 MeV to 399 MeV. The A2 data (violet markers) are compared to the MAID2007 prediction (black lines), with a good agreement.

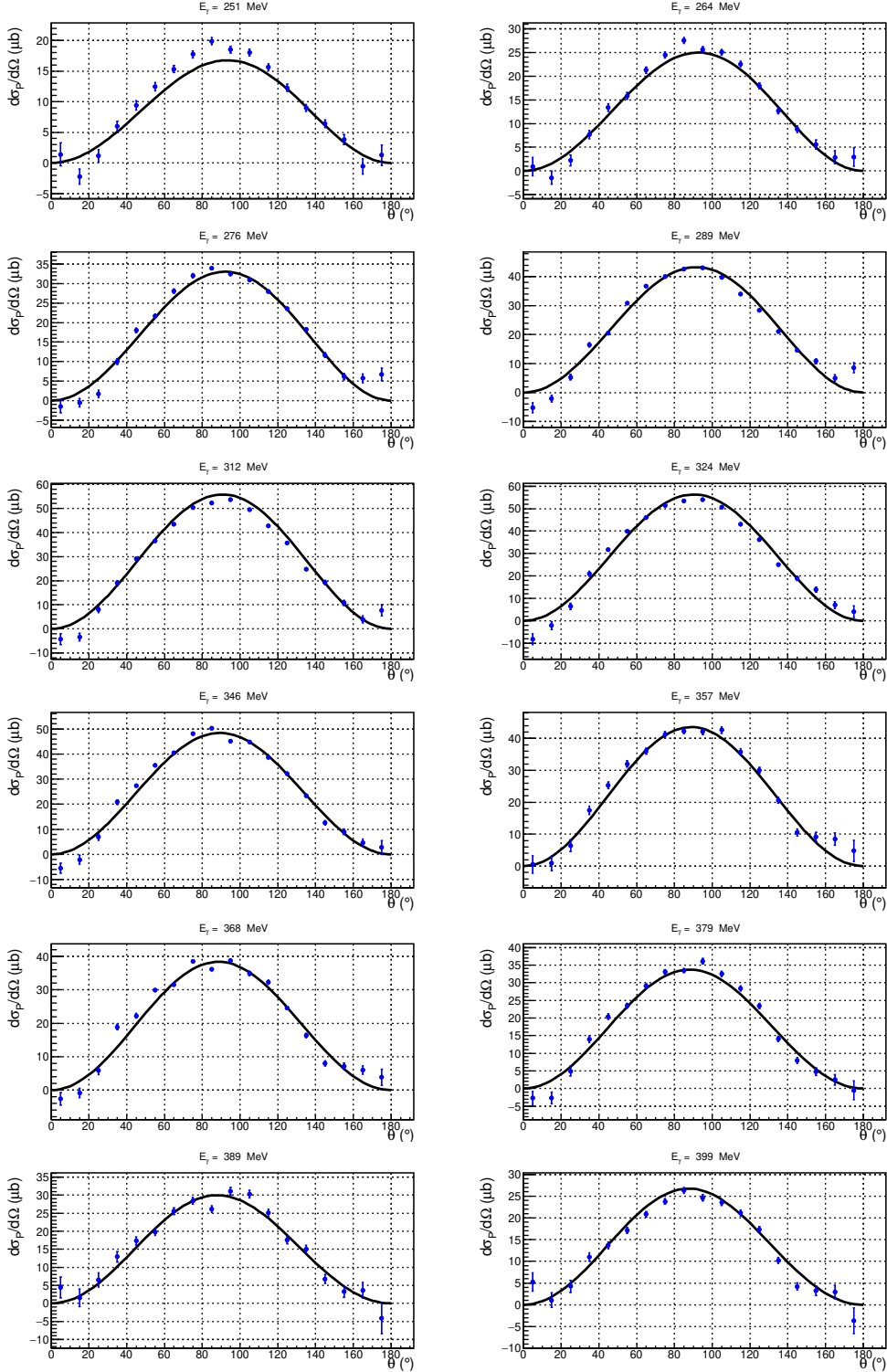


Figure 4.5: Parallel differential cross section (blue markers) resulting from the formula 4.3. The data are compared to the MAID2007 model (black lines).

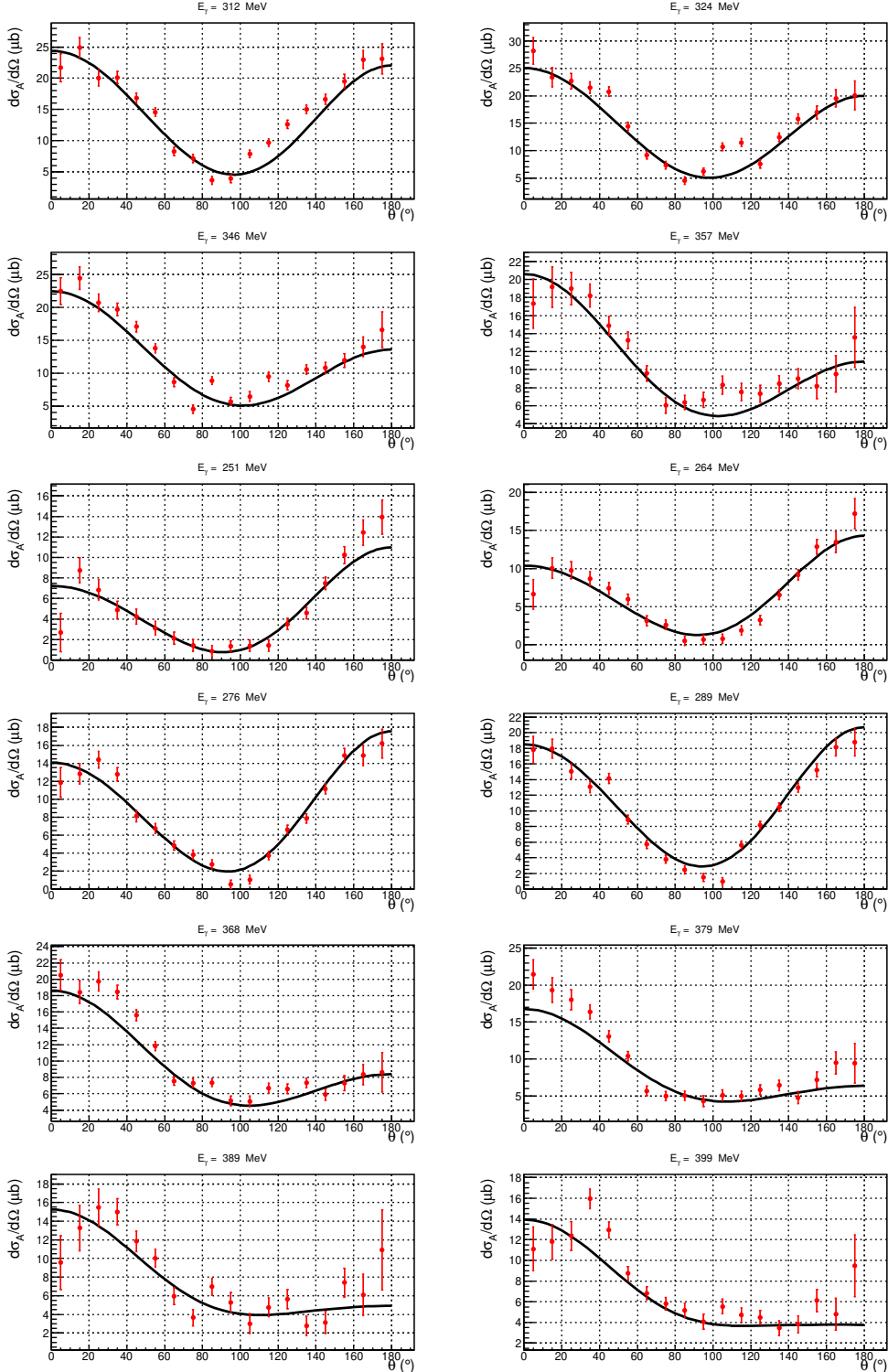


Figure 4.6: Antiparallel differential cross section (red markers) resulting from the formula 4.3. The data are compared to the MAID2007 model (black lines).

momentum conservation law gives rise to strict selection rules about the multipoles emitted or absorbed in particular transitions.

In Figure 4.7, the proton and the $\Delta(1232)$ resonance are shown with their constituent quarks: the proton has both spin and isospin $S = I = \frac{1}{2}$ while the Δ has both spin and isospin of $S = I = \frac{3}{2}$. The $p - \Delta(1232)$ transition mainly results from the spin flip of one of the constituent quarks induced by a M1-photon absorption, which corresponds to the M_{1+} -multipole for the pion production. Nevertheless, the parity and angular momentum conservation laws make the $p - \Delta(1232)$ transition possible via the E2-photon absorption as well, i.e. via the E_{1+} -multipole. The electric quadrupole transitions are of particular interest because they give information on the particle charge distribution, pointing out oblate or prolate deformation of the baryon structure. For particles with spin $S < 1$, the quadrupole deformation can not be directly measured but it can be inferred through an accurate analysis of the transitions between ground state and excited states [4].

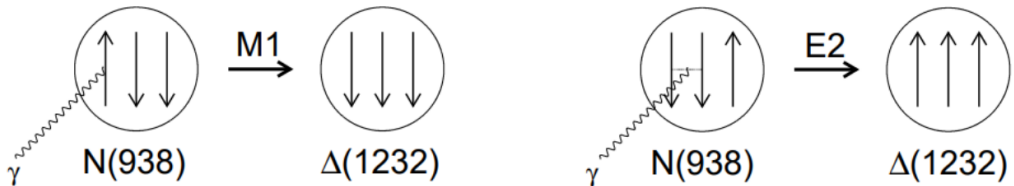


Figure 4.7: $p - \Delta(1232)$ transition via the magnetic dipole mechanism (on the left) and the electric quadrupole mechanism (on the right) [4].

4.3.1 E2/M1 ratio

The proton is primarily photo-excited by the magnetic dipole (M1) radiation, as Figure 1.4 shows; yet, since its wave function includes non-spherical d-wave components, the $p - \Delta(1232)$ transition also occurs in the presence of the electric quadrupole (E2) radiation [38]. To demonstrate that photon the electric quadrupole moment can be responsible of the $p - \Delta(1232)$ transition, the E2/M1 ratio, defined as [39]

$$R_{EM} = \frac{E2}{M1} = \frac{E_{1+}^{3/2}}{M_{1+}^{3/2}} \Big|_{\sqrt{s}=M_\Delta}, \quad (4.4)$$

must be studied in the resonance peak region in order to observe an E2 component in the $\Delta(1232)$ excitation. $E_{1+}^{3/2}$ and $M_{1+}^{3/2}$ are the quadrupole amplitudes corresponding to the absorption of the E2 and M1 photon multipoles respectively. The E2/M1 ratio for the $p - \Delta(1232)$ transition is an important quantity suggesting the presence of charge deformations in the baryon structure and, in particular, a non-zero negative value of the electric quadrupole transition moment implies an oblate charge distribution of the proton and the $\Delta(1232)$ [40].

The multipoles belonging to the MAID2007 model give as a result [39, 41]:

$$R_{EM} = -(2.5 \pm 0.1_{stat} \pm 0.2_{sys})\%. \quad (4.5)$$

The experimental R_{EM} value has been calculated by changing the $E_{1+}^{3/2}$ contribution to the P_{33} resonance (i.e to the $\Delta(1232)$ excitation) in the MAID2007 webpage [14]. Three different values has been set: $E_{1+}^{3/2} = 0.00$, $E_{1+}^{3/2} = 1.00$ and $E_{1+}^{3/2} = 2.00$.

$E_{1+}^{3/2} = 1.00$ is the “expected” value, corresponding to a -2.5% contribution of $E_{1+}^{3/2}$ relative to $M_{1+}^{3/2}$; $E_{1+}^{3/2} = 0.00$ and $E_{1+}^{3/2} = 2.00$ are associated with a 0% (no $E_{1+}^{3/2}$ contribution to the transition) and a -5% $E_{1+}^{3/2}$ contribution respectively.

Figure 4.8 shows, for three different energy values in the $\Delta(1232)$ region, the antiparallel cross section component, the most sensible to $E_{1+}^{3/2}$ variations. While the $M_{1+}^{3/2}$ multipole dominates the parallel cross section, it does not contribute at all to the antiparallel one. The $d\sigma_A/d\Omega$ cross section is therefore suitable to the study of $E_{1+}^{3/2}$ variations because, being the $M_{1+}^{3/2}$ multipole absent, even the small contribution of other multipoles is directly detectable. The blue, black and green lines represent the MAID2007 model predictions for $E_{1+}^{3/2} = 0.00$, $E_{1+}^{3/2} = 1.00$ and $E_{1+}^{3/2} = 2.00$.

With the maximum likelihood (ML) method, the minimum of the χ^2 function [42],

$$\chi^2 = \sum_{i=1}^n \frac{(m_i - d_i)^2}{\sigma_{d,i}^2}, \quad (4.6)$$

among the three different $E_{1+}^{3/2}$ contributions has been found; m_i and d_i represent the model and data values, respectively, and $\sigma_{d,i}^2$ is the data squared error.

The χ^2 values for different $E_{1+}^{3/2}$ contributions are displayed in Figure 4.8. The minimum χ^2 value (χ_{min}^2) for $E_{1+}^{3/2} = 1.00$ confirms the -2.5% contribution of $E_{1+}^{3/2}$ to the $p - \Delta(1232)$ transition.

The R_{EM} value rising from this analysis is:

$$R_{EM} = -(2.5 \pm 0.28)\%, \quad (4.7)$$

compatible within the error with the MAID2007 value.

The R_{EM} error has been estimated by using a standard method for the calculation of the χ^2 confidence interval (CI). The CI with an half width equal to one standard deviation is determined to be $\chi^2 \pm 1$, with a confidence level (CL) of $\sim 68.3\%$ [42]. The error has thus been evaluated by taking the difference between the $E_{1+}^{3/2}$ values corresponding to χ_{min}^2 and $\chi_{min}^2 + 1$.

A good agreement between the model predictions and the accomplished analysis has been achieved.

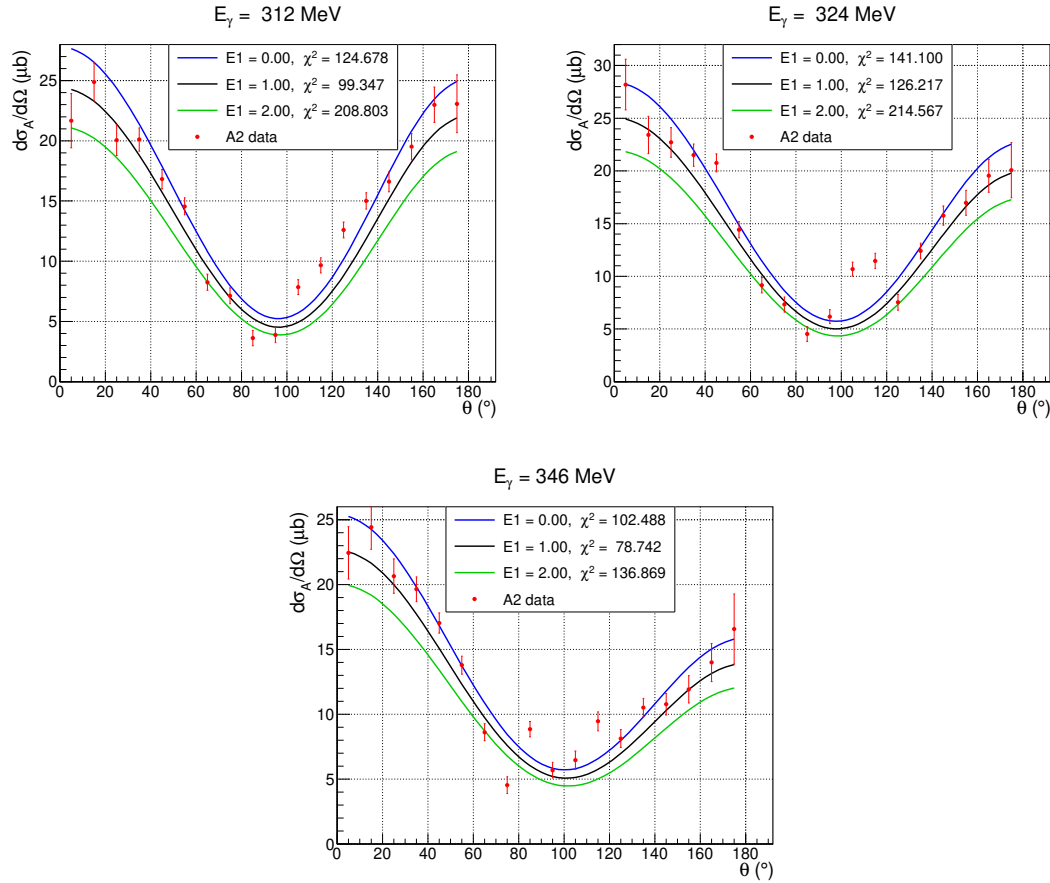


Figure 4.8: The antiparallel cross section component is shown for three different energy values in the $\Delta(1232)$ region. The blue, black and green lines represent the MAID2007 model predictions for $E_{1+}^{3/2} = 0.00$, $E_{1+}^{3/2} = 1.00$ and $E_{1+}^{3/2} = 2.00$. The χ^2 values for different $E_{1+}^{3/2}$ contributions are displayed too.

Conclusions

The analysis performed for this Master's thesis work is part of a large series of measurements carried out by the A2 collaboration at MAMI, in Mainz (Germany), with the aim to extend and improve the current understanding of the nuclear and subnuclear structure and dynamics. In particular, the present results provide a valuable input to the study of the proton and its $\Delta(1232)$ resonance via the study of neutral pion photoproduction reactions. The datasets analyzed in this work were collected at the tagged photon facility of the MAMI accelerator, using unpolarized and linearly polarized photon beams on an unpolarized liquid hydrogen target.

The cross section for the total inclusive $\gamma p \rightarrow X$ reaction is presented and compared with a good agreement with the published results of MacCormick et al. [35]. The analyzed data provide new precise results of the total and differential unpolarized cross sections for the $\gamma p \rightarrow \pi^0 p$ reaction. They are compared to the MAID2007 model predictions, showing a generally good agreement both for the dataset obtained with the unpolarized and the linearly polarized photon beam. These data are increasing the available statistics, hence providing an important testing ground for the existing models.

By using the results of the doubly-polarized $\vec{\gamma}\vec{p} \rightarrow \pi^0 p$ reaction, analyzed within the A2 collaboration, the differential cross sections for the different spin configurations, parallel $d\sigma_{3/2}/d\Omega$ and antiparallel $d\sigma_{1/2}/d\Omega$, have been extracted separately. The results are compared with the MAID2007 model predictions with a good agreement.

Furthermore, the electric quadrupole to the magnetic dipole ratio, $R_{EM} = E2/M1$, has been calculated. The obtained value $R_{EM} = -(2.5 \pm 0.28)\%$, within the error, is compatible with the MAID2007 value. Additional efforts should be still done to evaluate more precisely the value of the tagging efficiency, and so improving the photon flux

normalization, and to carefully estimate the systematic errors.

Acknowledgements

I would like to thank my supervisor Susanna Costanza for her valuable help in these last months. You have taken responsibility for me and for my work. Thank you for having hosted me in your office and thank you for your tips. I am grateful for your support.

I want to thank Edoardo Mornacchi with all my heart. From the very beginning you have always been by my side and without your help none of this would have been possible. You are a good and patient teacher and I learnt a lot from you. During my time in Mainz, I had a great time with you. I will never forget the beers along the Rhein side, your funny T-shirts, the night shifts spent together and your melt coffee maker.

A special thank goes to Prof. Paolo Pedroni. You are the mastermind behind this work and I owe you the two greatest chances of my life of living and working abroad. Thank for having always been available and ready to answer to my questions.

I want also to thank every single member of the A2 collaboration, you are a small but an amazing family. In particular, I want to thank Federico Cividini who made me love Mainz two years ago and, since then, I look forward for coming back again.

References

- [1] M. Thomson, *Modern Particle Physics.* Cambridge University Press, *DOI:* 10.1017/CBO9781139525367, 2013.
- [2] R. Gupta, “Introduction to Lattice QCD,” *arXiv:hep-lat/9807028*, 1998.
- [3] R. A. Briceno *et al.*, “Scattering processes and resonances from Lattice QCD,” *Rev.Mod.Phys.* **90** (2018) no.2, 025001, *DOI* 10.1103/RevModPhys.90.025001, 2018.
- [4] B. Krusche and S. Schadmand, “Study of non-strange baryon resonances with meson photoproduction,” *Progress in Particle and Nuclear Physics, Volume 51, Issue 2, p. 399-485*, *DOI:* 10.1016/S0146-6410(03)90005-6, 2003.
- [5] K. Hagen, *Particles and quantum fields.* World Scientific, *DOI:* 10.1142/9915, 2016.
- [6] A. Anisovich *et al.*, “Partial wave decomposition of pion and photoproduction amplitudes,” *Eur. Phys. J. A* (2005) **24:** 111, *DOI:* 10.1140/epja/i2004-10125-6, 2005.
- [7] G. F. Chew *et al.*, “Relativistic dispersion relation approach to photomeson production,” *Phys.Rev.* **106** (1957) 1345-1355, *DOI:* 10.1103/PhysRev.106.1345, 1957.
- [8] O. Hanstein, “Multipole analysis of pion photoproduction based on fixed t dispersion relations and unitarity,” *Nucl.Phys. A632* (1998) 561-606, *DOI:* 10.1016/S0375-9474(98)00818-5, 1997.
- [9] S. Costanza, “Doubly-polarised pion photoproduction on the nucleon at MAMI,” *The European Physical Journal Conferences* **142:01008**, *DOI:* 10.1051/epj-conf/201714201008, 2017.

- [10] I. S. B. et al, “Complete experiments in pseudoscalar photoproduction,” *Nucl. Phys. B95* (1975) 347-356, DOI: 10.1016/0550-3213(75)90049-8, 1975.
- [11] W. T. Chiang and F. Tabakin, “Completeness Rules for Spin Observables in Pseudoscalar Meson Photoproduction,” *Phys. Rev. C55* (1997) 2054-2066, DOI: 10.1103/PhysRevC.55.2054, 1997.
- [12] D. Griffiths, *Introduction to quantum mechanics*. Cambridge University Press, DOI: 10.1017/9781316995433, 1994.
- [13] D. Drechsel *et al.*, “Unitary isobar model - MAID 2007,” *Eur. Phys. J. A.* 34(1), DOI: 10.1140/epja/i2007-10490-6, 2007.
- [14] Mainz MAID webpage: <https://maid.kph.uni-mainz.de/maid2007/polariz.html>.
- [15] N. Valle, “Studio delle proprietà delle risonanze barioniche attraverso reazioni di fotoproduzione pionica,” Master’s thesis, University of Pavia, Italy, 2017.
- [16] D. Watts, “The Crystal Ball and TAPS detectors at the MAMI electron beam facility,” <https://www2.ph.ed.ac.uk/nuclear/photo/calorproceedings.pdf>.
- [17] C. Collicott, *Probing proton structure through single polarization observables of compton scattering and π^0 photoproduction within the $\Delta(1232)$ region*. PhD thesis, Dalhousie University, Halifax, Nova Scotia, 2015.
- [18] A. Jankowiak, “The Mainz Microtron MAMI - Past and Future,” *Eur. Phys. J. A.* 28(S1), DOI: 10.1140/epja/i2006-09-016-3, 2006.
- [19] K. Livingston, “The Stonehenge technique. A method for aligning coherent bremsstrahlung radiators,” *Nuclear Instruments and Methods in Physics Research. A603*(3), pp. 205-213, DOI: 10.1016/j.nima.2009.02.010, 2008.
- [20] A. Thomas, “Crystal Ball Hydrogen (Deuterium) Target manual.” A2 collaboration, 2004.
- [21] E. Mornacchi, “Studio della dipendenza dall’elicità della sezione d’urto della reazione $\gamma p \rightarrow n\pi^+$,” Master’s thesis, University of Pavia, Italy, 2014.

- [22] B. Nefkens, “The Crystal Ball Technical Report,” *UCLA*, 1995.
- [23] P. P. Martel, *Measuring proton spin polarizabilities with polarized Compton scattering*. PhD thesis, University of Massachusetts, USA, 2013.
- [24] W. R. Leo, *Techniques for Nuclear and Particle Physics Experiments*. Springer, DOI: 10.11119/1.16209, 1994.
- [25] A2Wiki webpage:
<https://www.a2.kph.uni-mainz.de/intern/daqwiki/experiment/detectors>.
- [26] G. Audit *et al.*, “DAPHNE: a large-acceptance tracking detector for the study of photoreactions at intermediate energies,” *Nuclear Instruments and Methods in Physics Research A* **301** (1991) 473-481, DOI: 10.1016/0168-9002(91)90013-G, 1991.
- [27] D. R. Paudyal, *Spin polarizability of a proton using polarized photon beam and polarized butanol target at Mainz Microtron*. PhD thesis, University of Regina, Saskatchewan, Canada, 2017.
- [28] GitHub Acqu source: <https://github.com/A2-Collaboration/acqu>.
- [29] J. Annand, “Data Analysis within an AcquRoot Framework,” *Univeristy of Glasgow, UK*, 2008.
- [30] R. Brun and F. Rademakers, “ROOT - an Object Oriented Data Analysis Framework,” *Phys. Res. A* **389** (1997) 81-86, DOI: 10.1016/S0168-9002(97)00048-X, 1996.
- [31] M. Tanabashi and others (Particle Data Group collaboration), “Review of particle Physics,” DOI: 10.1103/PhysRevD.98.030001, 2019.
- [32] GitHub A2Geant webpage: <https://github.com/A2-Collaboration/A2Geant4>.
- [33] S. Agostinelli *et al.*, “Geant4 — a simulation toolkit,” *Nucl.Instrum.Meth. A* **506** (2003) 250-303, DOI: 10.1016/S0168-9002(03)01368-8, 2003.
- [34] Geant4 webpage: <https://geant4.web.cern.ch/>.

- [35] M. MacCormick *et al.*, “Total photoabsorption cross sections for ^1H , ^2H , and ^3He from 200 to 800 mev,” *Phys. Rev. C* 53, 41, DOI: 10.1103/PhysRevC.53.41, 1996.
- [36] George Washington University webpage:
http://gwdac.phys.gwu.edu/analysis/pr_analysis.html.
- [37] H. Stegen *et al.*, “Hadron polarizability data analysis: GoAT,” *AIP Conference Proceedings* 1697, 080003, DOI: 10.1063/1.4937698, 2015.
- [38] A. Blomberg *et al.*, “Electroexcitation of the $\Delta^+(1232)$ at low momentum transfer,” *Phys.Lett. B* 760 (2016) 267-272, DOI: 10.1016/j.physletb.2016.06.076, 2015.
- [39] R. Beck *et al.*, “Determination of the E2/M1 ratio in the $\gamma \text{ N} \rightarrow \Delta(1232)$ transition from a simultaneous measurement of $p(\gamma, p)\pi^0$ and $p(\gamma, \pi^+)n$,” *American Physical Society*, DOI: 10.1103/PhysRevC.61.035204, 2018.
- [40] T. Watabe *et al.*, “E2/M1 ratio for the $\gamma \text{ N} \rightarrow \Delta$ transition in the chiral quark soliton model,” *Phys Rev Lett.* 1987 Aug 10;59(6):624-626, DOI: 10.1103/PhysRevLett.59.624, 1995.
- [41] Particle Data Group webpage: <http://pdg.lbl.gov/2018/listings/rpp2018-list-Delta-1232.pdf>.
- [42] A. Rotondi, P. Pedroni, and A. Pievatolo, “Probabilità, statistica e simulazione,” *Springer, 3rd Edition*, DOI: 10.1007/b138380, 2004.